

The correlation between photometric variability and radial velocity jitter [★]

based on TESS and HARPS observations

S. Hojjatpanah^{1,2}, M. Oshagh^{3,4,1}, P. Figueira^{5,1}, N.C. Santos^{1,2}, E. M. Amazo-Gómez^{6,4}, S. G. Sousa¹, V. Adibekyan^{1,2}, B. Akinsanmi^{1,2,7}, O. Demangeon¹, J. Faria¹, J. Gomes da Silva¹, and N. Meunier⁸

¹ Instituto de Astrofísica e Ciências do Espaço, Universidade do Porto, CAUP, Rua das Estrelas, 4150-762 Porto, Portugal e-mail: Saeed.Hojjatpanah@astro.up.pt

² Departamento de Física e Astronomia, Faculdade de Ciências, Universidade do Porto, Rua Campo Alegre, 4169-007 Porto, Portugal

³ Instituto de Astrofísica de Canarias (IAC), E-38200 La Laguna, Tenerife, Spain

⁴ Institut für Astrophysik, Georg-August-Universität, Friedrich-Hund-Platz 1, 37077 Göttingen, Germany

⁵ European Southern Observatory, Alonso de Cordova 3107, Vitacura, Santiago, Chile

⁶ Max-Planck-Institut für Sonnensystemforschung, Göttingen, Germany

⁷ National Space Research and Development Agency, Airport Road, Abuja, Nigeria

⁸ Univ. Grenoble Alpes, CNRS, IPAG, F-38000 Grenoble, France

Received —, —; accepted —, —

ABSTRACT

Context. Characterizing the relation between stellar photometric variability and radial velocity (RV) jitter can help us to better understand the physics behind these phenomena. The current and upcoming high precision photometric surveys such as TESS, CHEOPS, and PLATO will provide the community with thousands of new exoplanet candidates. As a consequence, the presence of such a correlation is crucial in selecting the targets with the lowest RV jitter for efficient RV follow-up of exoplanetary candidates. Studies of this type are also crucial to design optimized observational strategies to mitigate RV jitter when searching for Earth-mass exoplanets.

Aims. Our goal is to assess the correlation between high-precision photometric variability measurements and high-precision RV jitter over different time scales.

Methods. We analyze 171 G, K, and M stars with available TESS high precision photometric time-series and HARPS precise RVs. We derived the stellar parameters for the stars in our sample and measured the RV jitter and photometric variability. We also estimated chromospheric Ca II H & K activity indicator $\log(R'_{HK})$, $v \sin i$, and the stellar rotational period. Finally, we evaluate how different stellar parameters and an RV sampling subset can have an impact on the potential correlations.

Results. We find a varying correlation between the photometric variability and RV jitter as function of time intervals between the TESS photometric observation and HARPS RV. As the time intervals of the observations considered for the analysis increases, the correlation value and significance becomes smaller and weaker, to the point that it becomes negligible. We also find that for stars with a photometric variability above 6.5 ppt the correlation is significantly stronger. We show that such a result can be due to the transition between the spot-dominated and the faculae-dominated regime. We quantified the correlations and updated the relationship between chromospheric Ca II H & K activity indicator $\log(R'_{HK})$ and RV jitter.

Key words. Planetary systems, Planets and satellites: detection, Techniques: radial velocities, spectroscopy, photometric, Stars: activity

1. Introduction

Detecting and accurately characterizing low-mass exoplanets is a challenge for observational astronomy. Besides instrumental limitations, one of the main remaining obstacles is the intrinsic stellar variability, often called "jitter" in the exoplanet's field. The two main detection methods, radial velocity (RV) and transit photometry, struggle with the impact of stellar activity induced signal (e.g., Oshagh 2018), which is generated by active regions, such as spots and plagues, associated to strong magnetic fields. The presence of active regions on a rotating star not only gener-

ates RV jitter but also induces photometric modulations in transit observations (e.g., Czesla et al. 2009; Oshagh 2018).

Stellar activity can both mimic RV planetary signals (similar to planetary signals) and hide a real planetary signal by adding significant stellar activity induced signal. (e.g., Saar et al. 1998; Dumusque et al. 2011b,a; Queloz et al. 2001; Santos et al. 2002, 2010; Boisse et al. 2011; Santos et al. 2014; Díaz et al. 2016). Moreover, it can degrade the precision of the planetary parameters derived through RV (e.g., Cloutier et al. 2018; Fischer et al. 2016) or transit measurements (Czesla et al. 2009; Oshagh et al. 2013a,b; Barros et al. 2014; Oshagh et al. 2015).

Huélamo et al. (2008) and Figueira et al. (2010) demonstrated that the stellar spots can even reproduce the RV variations as high as those produced by giant planets on short orbits. Additionally, Robertson et al. (2014) showed that the activity can

[★] Based on observations collected at the La Silla Observatory, ESO(Chile), with the HARPS spectrograph at the 3.6-m telescope. See the acknowledgements for the list of specific programs.

masquerade as a planet located inside the habitable zone of M dwarfs.

It has further been shown that the stellar photometric variability is correlated with the RV jitter (e.g., [Aigrain et al. 2012](#); [Bastien et al. 2014](#); [Oshagh et al. 2017](#)). Defining such relations as precisely as possible is crucial in optimizing the telescope time invested in the RV follow-up of upcoming planetary candidates from ongoing and upcoming missions such as TESS ([Ricker et al. 2014](#)) and PLATO ([Rauer et al. 2014](#)) with high-resolution spectrographs, such as HARPS ([Mayor et al. 2003](#)) and ESPRESSO ([Pepe et al. 2014](#)). Several studies have attempted to assess this potential correlation. [Bastien et al. \(2014\)](#) compared the variability in Kepler light-curves and the root-mean-square (RMS) of RV time series of twelve G and K stars. They did not find any strong correlation between the RV-RMS and the amplitude of photometric variability. Instead, they found a correlation between the number of significant peaks in the Lomb-Scargle periodograms of the light-curves and the RMS of stellar RV.

Later, [Cegla et al. \(2014\)](#) studied a sample of 900 stars using GALEX ([Martin et al. 2005](#)) and Kepler surveys ([Borucki et al. 2010](#)). They estimated the chromospheric activity index of each target using the UV flux measured by GALEX ([Findeisen et al. 2011](#)) and used it to calculate the RV jitter by using empirical relations reported in several studies ([Santos et al. 2000](#); [Wright 2005](#); [Saar et al. 2003](#)). For magnetically quiet stars, they found a strong correlation between photometric variability and the estimated RV jitter. They also evaluated the correlation between RV jitter and F_8 ¹ ([Bastien et al. 2013](#)) and additionally with the number of zero crossings (X0) in photometric observation. They found that the correlation between RV jitter and F_8 is sensitive to the effective temperature of the stars.

[Oshagh et al. \(2017\)](#) performed an intensive study on a sample of nine stars with different levels of activity. They obtained simultaneous K2 photometric light-curves and HARPS RV measurements. From these observations the photometric variability, F_8 , RV jitter, spectroscopic activity indicators BIS, FWHM, and $\log(R'_{HK})$ were derived. The authors found that a strong correlation exists between RV jitter and photometric variation for highly active stars ($\log(R'_{HK}) \geq -4.66$). Moreover they found that for highly active stars strong correlations exist between RV jitter and variability of activity indicators, such as BIS, FWHM, and $\log(R'_{HK})$. The authors pointed out that all of these correlations become weaker for stars with low-amplitude photometric variations and for slowly-rotating stars. The same study also showed that even though F_8 has a strong correlation with the RV jitter, it does not display a strong correlation with rotationally-induced photometric variability. They also confirmed the evidence of the two spot-dominated and plage-dominated regimes presented in several other studies ([Lockwood et al. 1997](#); [Radick et al. 1998](#); [Shapiro et al. 2016](#)).

Recently, [Tayar et al. \(2019\)](#) investigated the relationship between stellar properties (such as $\log g$, temperatures, and metallicities) and convective granulation using F_8 . They used a large sample of dwarfs, subgiants and red giants (2465 stars in total) observed by Kepler and APOGEE surveys. With their study, they updated the relationship between convective granulation and stellar properties. Using the empirical Flicker-jitter relations presented by ([Bastien et al. 2014](#); [Oshagh et al. 2017](#)), they pre-

dicted the granulation-driven RV jitter amplitudes for a sample of stars observed by TESS.

The main objective of the current study is to extend these studies to explore, in unprecedented detail, the existence of correlations between RV jitter and photometric variability measurements. This study is performed for 171 G, K and M dwarfs observed with the high-resolution and stable spectrograph HARPS and with the TESS mission, which both provide some of the best RV and photometric precision available.

This paper is organized as following: we explain the target selection and data reduction in Sect. 2. The derivation of stellar parameters is described in Sect. 3. In Sect. 4, we analyze the correlation between RV jitter and photometric peak-to-peak variation. The application of our obtained result on TESS planet candidate host stars is presented in Sect. 6 by identifying the potential targets which will have the lowest RV jitter based on their light curve photometric variability. Finally, conclusions are drawn in Sect. 7.

2. Target selection and data reduction

2.1. Target selection

We selected our targets by applying the following criteria:

- I. Cross matching the stars in the HARPS archive with those observed by TESS during its first year (covering 13 observation sectors in the Southern Ecliptic Hemisphere)². All targets have their RV and photometric observations publicly available in the ESO archive and Mikulski Archive for Space Telescopes (MAST)³, respectively.
- II. Selecting only the stars with RV measurements taken after the fiber change of HARPS on June 2015 ([Lo Curto et al. 2015](#)) to avoid offset in RV measurements and to make the RV measurements as homogeneous as possible.⁴
- III. Removing the targets with known exoplanets to eliminate RV variations due to the known companions⁵.
- IV. Selecting stars with measurements on at least 5 nights over a minimum period of one week.⁶ This criterion aims at producing a minimum sampling of the rotation modulation of G, K and M dwarfs ([Nielsen et al. 2013](#); [Reinhold & Hekker 2020](#)).

A total of 171 stars satisfy all of the above criteria. They are all listed in Table. C.1. In Fig. 1, we illustrated the TESS observation windows (sectors) and RV measurement epochs of each target.

2.2. Light curve: TESS

We obtained the light-curves of all 171 stars from MAST. MAST contains simple aperture photometry (SAP_flux) ([Morris et al. 2017](#)) as well as presearch data conditioning (PDCSAP_flux).

² <https://tess.mit.edu/observations/>

³ <https://archive.stsci.edu>

⁴ Including the data before the fiber change would add few points per star and one free parameter, the offset between the two, which brings only a little gain.

⁵ <https://exoplanetarchive.ipac.caltech.edu/exoplanet.eu>

⁶ We have applied this criteria on the reduced final RV measurements which we explained in Sect. 2.3

¹ F_8 is the RMS of photometric light-curve on timescale shorter than 8 hr, and has been shown to also correlate strongly with the stellar $\log g$.

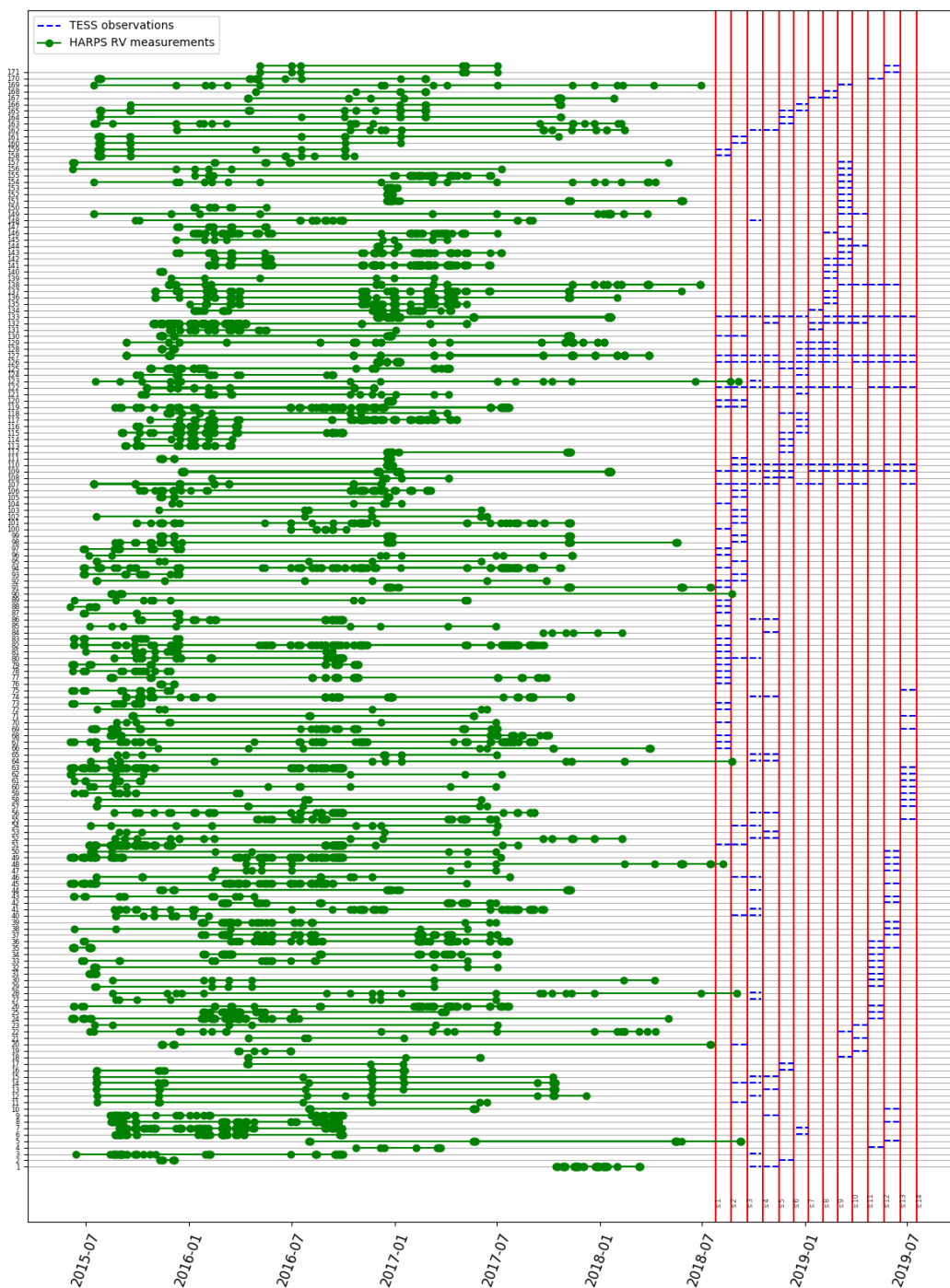


Fig. 1: Total RV measurements and TESS observation windows. The green points show the RV measurements dates. Blue dash and red vertical lines show the TESS observations and sectors, respectively. The name of each star is presented in Table. C.1 using index number in y-axis.

Most of the targets (96 %) were observed in only one TESS sector. For stars with light-curves in two or more consecutive sectors, we merged all available light-curves. We used quality-flag⁷ as suggested by the TESS Data Product review, also recently used and tested in (Vida et al. 2019). We used SAP_flux which optimizes the aperture for the best signal-to-noise for each target (Bryson et al. 2017) and also the calibrated pixels in order

to perform a summation of the flux. The SAP light curves provided by the TESS pipeline are also background corrected. We removed outlier flux points using a sigmaclipping of three standard deviations and smoothed the fluxes using Savitzky-Golay filter within 15 data point windows (~ 30 minutes) to reduce the effect of the short-time scale photometric variability. Since we are interested in variability at stellar rotation timescales, this smoothing does not affect our results. We then normalized the flux by the median flux values. We derived the ratio between the peak-to-peak of light curve variability of SAP_flux and the peak-

⁷ 101010111111: <https://outerspace.stsci.edu/display/TESS/2.0+-+Data+Product+Overview>

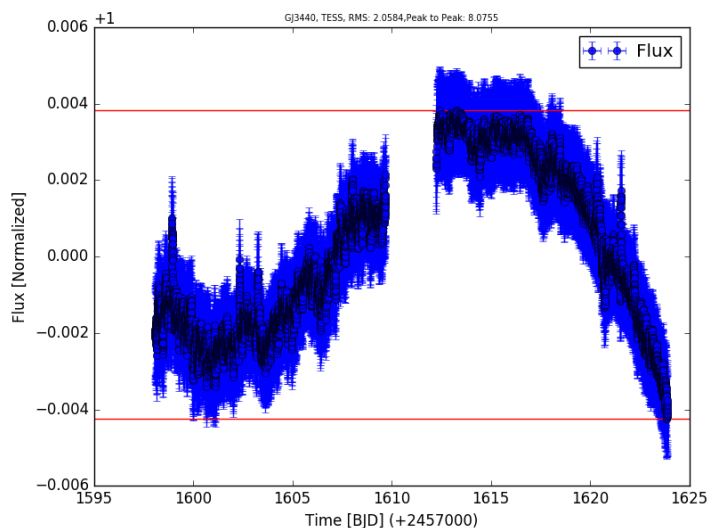


Fig. 2: Example of light curve of GJ3440 during one TESS sector (blue points) and the red lines presenting the peak-to-peak of light curve.

to-peak of light curve variability of PDCSAP_flux. If this ratio was larger than 3.0, we checked the light curves visually to ensure if there was any evidence for systematic errors in SAP_flux. For more than 90 % of the stars, we used SAP_flux, and for the rest we assumed that the light-curves are dominated by systematic errors therefore we used PDCSAP_FLUX. In Fig. 2, you can see a sample of reduced light curve in one sector for one star.

2.3. HARPS RVs

For the 171 stars selected in Section 2 we collected the available HARPS data through ESO archive⁸. The data were reduced using the official HARPS pipeline (DRS), that delivers the RV and full width at half maximum (FWHM) measured on each Cross-Correlation Function (CCF). We determined the significant outliers of the RV time-series by applying a sigma-clipping of three standard deviations, and removed the few measurements that show an RV error larger than 9 m s^{-1} as an admittedly arbitrary value. This threshold was set for being significantly larger than the median RV error ($\sim 0.80 \text{ m s}^{-1}$) for the whole sample. After the nightly binning of the data, in total, over 3971 spectra were collected and 81 RV measurements ($\sim 2\%$) were removed based on the previous outlier and photon noise criteria. For each star, we subtracted the mean value of the RV from the RV measurements. Moreover, we corrected for linear long term RV trends using a linear fit for 27 stars of our sample⁹. This linear trend removal was done to ensure eliminating the signal from any possible unknown long period companions around our targets. It is worth mentioning that unknown planets on short orbits could also affect our RV-RMS measurements, however, if undiscovered and passing the previous vetting criteria, it means that they must be low mass planets and induce low RV semi-amplitude, and thus they do not affect

⁸ https://www.eso.org/sci/observing/phase3/data_streams.html

⁹ GJ3440, HD021175, HD107094, HD1388, HD16548, HD185283, HD19230, HD19641, HD200133, HD202917, HD205536, HD207129, HD211415, HD213042, HD218860, HD221638, HD222335, HD28471, HD3074A, HD40397, HD42936, HD6107, HD76849, HD88218, HD89839, HD94771, HD96700

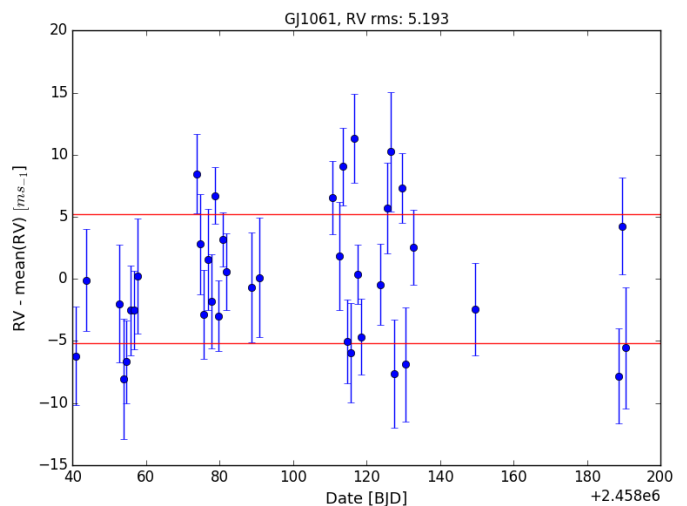


Fig. 3: Example of RV measurements for GJ1061 (blue dots), and the red lines presenting the \pm RV-RMS values.

our study significantly. In Fig. 3, we present an example of final RV time-series of one star as well as its associated RV-RMS measurement. Minimum, maximum, and the average of the time spans of the RV observations are ~ 7 days, ~ 3 years, and 1.5 years, respectively. The histogram of the RV time spans is presented in Fig. B.4.

2.4. Subsamples

The HARPS measurement are not contemporaneous with TESS observations. Since stellar activity patterns are expected to evolve with time, we divided our whole sample into 4 subsamples as a function of time lag between TESS and HARPS. For the first subsample we considered only the stars with RVs measured up to one year prior to the TESS observations, hereafter named as “year 1”. The second subsample contains the stars that have RV measurements in a time interval from one year to two years before TESS observations, hereafter named as “year 2”; the same criteria were used to create the third and the fourth subsamples hereafter named as “year 3” and “year 4”, respectively. Thus, it is important to emphasize that we divided all the RV measurements into four subsamples, and some stars are present in more than one subsample. According to our criteria for dividing the whole RV measurements into the four subsamples, few stars were not categorized in any of these four subsamples, and are only considered in the whole sample. Despite the ability for a star to appear in multiple subsamples, the RV-RMS for a star in a given subsample only uses the RVs taken during that subsample’s time-frame. The samples in which targets are present is listed in Table. C.1; stars which are used only in whole sample are labeled as “w”.

3. Stellar parameters

Accurate stellar parameters are necessary for the characterization of exoplanets and their hosts (Mayor et al. 2004; Fischer & Valenti 2005; Reffert et al. 2015; Adibekyan et al. 2018). Stellar parameters rule the physics behind the generation of stellar activity regions, and are thus of interest in this analysis. Therefore, we derived the main spectroscopic stellar parameters: effective tem-

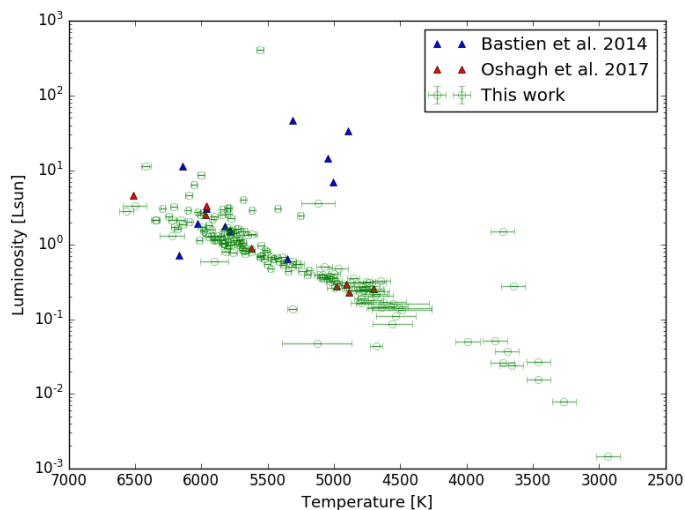


Fig. 4: HR diagram for the sample of stars used in this work.

perature (T_{eff}), metallicity ([Fe/H]), surface gravity ($\log g$) and stellar rotation rate for the stars in our sample. The stellar parameters for G and K dwarfs are determined with the procedure described in Sousa (2014). For the M dwarfs in the sample, we used a modified version of the method and software developed by Neves et al. (2014)¹⁰.

Fig. 4 presents the Hertzsprung–Russell diagram (HR), for the stars in our sample on which we over-plotted the samples that were used in the two similar previous studies (Oshagh et al. 2017; Bastien et al. 2014). Our sample size is one order of magnitude larger than the previous studies, and covers a wider range of effective temperatures for G and K dwarfs; however, the number of M-dwarfs in our sample is relatively small.

3.1. Chromospheric activity indicator $\log(R'_{HK})$ and $v \sin i$

We derived values for the S-index of each star to evaluate the chromospheric magnetic activity level and its evolution. We used the open source package *ACTIN*¹¹ (Gomes da Silva et al. 2018) to calculate the S_{CaII} index (Vaughan et al. 1978; Duncan et al. 1991) homogeneously for all individual spectra following the instructions in (Gomes da Silva et al. 2011; Hojjatpanah et al. 2019, and references therein). We then calibrated S_{CaII} to the Mt. Wilson scale using open source package *pyrhk*¹² and calculated the R'_{HK} chromospheric emission ratio as defined in Noyes et al. (1984).

For each star we created a $\log(R'_{HK})$ time-series and calculated the mean and peak-to-peak of variation of $\log(R'_{HK})$ to evaluate the variation of chromospheric activity during the observation span. In Fig. 5 we present the distribution of mean $\log(R'_{HK})$ as a function of spectral types. This figure shows that the majority of our stars are magnetically relatively similar to the solar average value of $\log(R'_{HK}) \sim -4.90$ (Mamajek & Hillenbrand 2008), which is a consequence of a bias in the target selection of stars for precise RV searches with HARPS.

It has been demonstrated that the RV jitter depends strongly on the projected rotational velocity ($v \sin i$) (e.g., Saar & Donahue 1997; Desort et al. 2007; Boisse et al. 2011; Korhonen et al.

¹⁰ <http://www.astro.up.pt/resources/mcal/Site/MCAL.html>

¹¹ <https://pypi.org/project/actin/>, <https://github.com/gomesdasilva/ACTIN>

¹² <https://github.com/gomesdasilva/pyrhk>

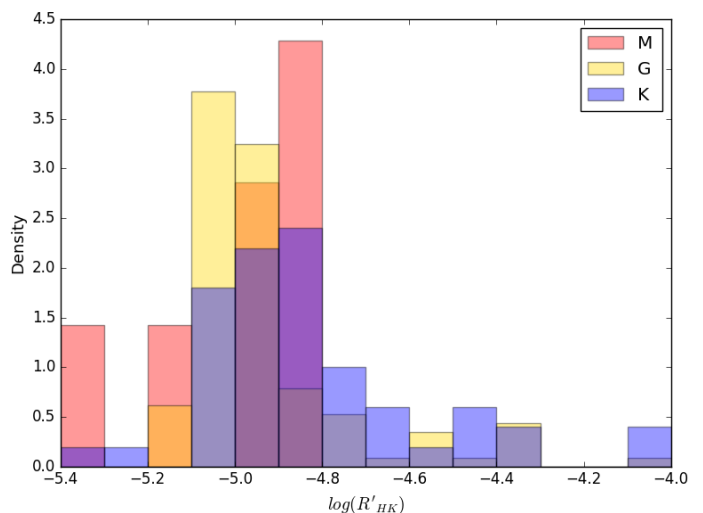


Fig. 5: Histogram of mean $\log(R'_{HK})$ for the sample of stars used in this work. Red, gold and blue correspond to the spectral type of the star, M, G and K respectively.

2015). Thus, we expect that $v \sin i$ should be one of the influential parameters in this investigation. Therefore, we estimated $v \sin i$ of all our stars based on the measured FWHM of the CCF. We used the procedure described in Santos et al. (2002); Maldonado et al. (2017); Hojjatpanah et al. (2019, and references therein).

3.2. Stellar rotation period

Photometric contrast differences associated to magnetic features (e.g., dark spots and bright faculae) generate traceable signatures of stellar rotation periods on light curves.

We analyze the presence of a periodic modulation signal from stellar rotation on the TESS photometric time-series using the gradient of the power spectra (GPS) (see Shapiro, A. I. et al. 2020; Amazo-Gómez et al. 2020). We successfully recover the rotation period for 71 out of 171 stars of the sample. We report the estimated rotation period from the GPS method in Table. C.1. The rotation period from GPS is determined from the enhanced profile of the high-frequency tail of the power spectrum. In particular, we identify the point where the gradient of the power spectrum GPS in log-log scale reaches its maximum value. Such a point corresponds to the high frequency inflection point (HFIP), that is, where the concavity of the power spectrum plotted in the log-log scale changes sign. The position of inflection point is related to the rotation period of star by the calibration factor α_{Sun} , for Sun-like stars.

For the calculations presented in this project we adopt a solar-like calibration factor $\alpha_{Sun} \pm 2\sigma = 0.158 \pm 0.014$, and 2 sigma uncertainty Shapiro, A. I. et al. (for more details see, 2020); Amazo-Gómez et al. (for more details see, 2020).

We also estimated the faculae to spot ratio for 29 of the 71 stars. Following Shapiro, A. I. et al. (2020); Amazo-Gómez et al. (2020); Amazo-Gomez, E.M. et al. (2020), the light curve is faculae dominated when the ratio between HFIP and the independent rotation period ranges between [0.11-0.16], and spot is dominated when the value falls between [0.16-1.24].

4. Correlation between RV jitter and photometric peak-to-peak

4.1. Correlation as a function of time

In Fig. 6 we present the RV-RMS versus peak-to-peak of the photometric time series for the four different subsamples. To evaluate the possible influence of stellar rotation velocity and its magnetic activity level variation, we code these variables into marker color and size.

In order to evaluate the strength of the correlation between RV-RMS and peak-to-peak of light curve, we derived two correlation coefficients. We used the Pearson's correlation coefficient (ρ_{pe}) that evaluates the presence of a linear relationship between data pairs, as well as Spearman's correlation coefficient (ρ_{sp}) that, working on ranked data, assesses the presence of a monotonic relationship. Both correlation coefficients were derived using the code described in Figueira et al. (2016) which uses the Bayesian framework to evaluate the significance of the presence of a correlation.

In each panel of Fig. 6 we also report the value of the ρ_{pe} correlation coefficient and its posterior distribution. For data obtained within year 1 time span, we obtained the correlation coefficient $\rho_{pe} = 0.989 \pm 0.005$ ($\rho_{sp} = 0.550 \pm 0.133$) for the correlation between photometric variability and RV jitter. As the time lag between RV measurement and TESS observation increases (subsample year 2, year 3 and year 4), the correlation becomes less strong and less significant. In the Table. 1, we presented the values of the ρ_{pe} and ρ_{sp} (Figueira et al. 2016). We also calculated the standard deviation and 95% Highest Posterior Density (HPD) Credible Interval as described in Figueira et al. (2016) for the both ρ_{pe} and ρ_{sp} values. As can be read on Table. 1 and Fig. 6, the correlation coefficients decrease to $\rho_{pe} = 0.848 \pm 0.033$ ($\rho_{sp} = 0.394 \pm 0.099$) for year 2 data, down to $\rho_{pe} = 0.520 \pm 0.071$ ($\rho_{sp} = 0.286 \pm 0.087$) and $\rho_{pe} = 0.331 \pm 0.109$ ($\rho_{sp} = 0.256 \pm 0.113$) for year 3 and year 4 data, respectively. ρ_{pe} is always larger than ρ_{sp} because of the extreme values in the subsets.

Therefore, our result shows that a correlation exists and decreases significantly when the time interval between the RV observations and photometric observation increases. This can be interpreted as a consequence of the magnetic activity cycles which lead to departure from periodic variability to a quasi-periodic variability, and thus result in weakening the correlation over time. This has an impact on the predictive ability of using one dataset to estimate the other: since several studies aimed at estimating the RV jitter using photometric measurements (e.g., Oshagh et al. 2017; Bastien et al. 2014), here we note that such a prediction after more than 2 years of photometric observation can be imprecise since the correlation between RV jitter and peak-to-peak light curve variability decreases ($\rho_{pe} \sim 0.8$ at year 2 to $\rho_{pe} \sim 0.5$ at year 3).

4.2. Overall correlation using the whole sample

The overall correlation between RV-RMS and peak-to-peak of light curve for the whole sample within the whole 4 years is presented in Fig. 7. The correlation is significant; The mean value of ρ_{pe} is 0.812 ± 0.026 and that of ρ_{sp} is 0.444 ± 0.061 . In this comparison it is important to mention that while the RV jitter is derived using relatively long-term observations (see Fig. B.4), the photometric peak-to-peak is measured during TESS observations, of roughly one month.

4.2.1. Functional form of the dependence

Careful inspection of the shape of the RV-RMS vs peak-to-peak photometry dependence in Fig. 7 (see also Fig. 6, especially the year 2 subplot), shows hints of a double behavior, a region where the dependence is weak or plateau (peak-to-peak of light curve variation < 6 ppt) and a region where the dependence is steeper, being associated to a stronger correlation coefficient (peak-to-peak of light curve variation > 6 ppt).

Here we aim to examine different functional forms that can properly describe the whole sample (Fig. 7) and individual subsamples (Fig. 6). To test this, we decided to fit RV jitter and photometric peak-to-peak variability using two types of functional models, a) a power law function and b) piecewise power law function (which is composed of two power law functions with a knee). We used Markov-chain Monte Carlo (MCMC) sampling using the library *emcee* (Foreman-Mackey et al. 2013) to perform the fit and obtain the uncertainties of the fitted parameters; for details refer to Appendix. A. The best fits are overplotted in Fig. 8 for year 2 which is closest subsampling group to the TESS observations with fairly sufficient number of data points. The best fits are also overplotted in Fig. 9 for the all RV sampling. All fitted parameters are reported in the Table. A.1. The best fit indicated with the Maximum a Posteriori (MAP).

We compare the best fitted models using RMS of the residual (RMS_{resi}) and Bayesian information criterion (BIC). For all the subsamples and also for the whole sample the BIC values are similar between two models. However, since the piecewise function is penalized for the two extra parameters, BIC values for the single power law function has lower BIC than piecewise function, which suggests that the single power law function as a better model, but with a low significant evidence. We considered BIC difference to be significant if $\Delta BIC > 10$ (Liddle 2007; Arevalo et al. 2017). On the other hand, for the subsample and also for the whole sample, the fits using piecewise model have lower RMS_{resi} , which means it can describe the data more precisely. For instance for the whole sample ($RMS_{resi} \sim 0.35$ vs 0.29) for single and piecewise model, respectively. If we consider the piecewise function as the best model for describing the data, the knee is located at a value of ~ 6.5 ppt peak-to-peak of light curve variation.

5. Correlations with activity level and rotational period

The large data-set presented here also allows us to explore other correlations that may be relevant for the estimation of RV jitter in different stars.

5.1. Correlation with $\log(R'_{HK})$

In the Fig. 10 and Fig. 11, we present the mean $\log(R'_{HK})$ values versus RV-RMS and peak-to-peak photometric variability for the whole sample. We also fitted the power law function and use MCMC to find the error in order to provide a relationship between the RV-RMS, peak-to-peak variability and $\log(R'_{HK})$ given by:

$$RV_{RMS} \propto (R'_{HK})^a, \quad a = 1.382_{-0.344}^{0.341}. \quad (1)$$

Our result is compatible with Saar et al. (2003) which reported $a = 1.1$ however less compatible with Santos et al. (2000) which reported $a = 0.55$. We obtained using the sample of stars in this

Time interval with TESS	ρ		95%		sample size
	ρ_{pe}	ρ_{sp}	ρ_{pe}	ρ_{sp}	
year 1	0.989 ± 0.005	0.550 ± 0.133	[0.979 0.996]	[0.287 0.791]	24
year 2	0.848 ± 0.033	0.394 ± 0.099	[0.782 0.908]	[0.196 0.578]	70
year 3	0.520 ± 0.071	0.286 ± 0.087	[0.384 0.656]	[0.120 0.456]	104
year 4	0.331 ± 0.109	0.265 ± 0.113	[0.111 0.531]	[0.043 0.486]	63
whole sample	0.812 ± 0.026	0.444 ± 0.061	[0.764 0.862]	[0.319 0.555]	171

Table 1: Result for Pearson’s correlation coefficient (ρ_{pe}) and Spearman’s rank-order correlation (ρ_{sp}) coefficient on ranked data, (Figueira et al. 2016) with ρ : correlation coefficient and its standard deviation and 95% highest posterior density (HPD) Credible Interval

project. If we assume that the same functional dependence exists between the $\log(R'_{HK})$ and peak-to-peak photometric we can write it as

$$LC_{pp} \propto (R'_{HK})^a, \quad a = 1.304_{-0.335}^{0.338}, \quad (2)$$

where LC_{pp} is peak-to-peak of light curve variation.

5.2. Correlation with stellar rotation period

In Top panel in Fig. 12, we present RV-RMS and the peak-to-peak light curve variation for the subsample of 71 stars with measured rotation periods (coded with marker size). The color bar represents the effective temperature. One can easily notice that stars with large RV-RMS and a large peak-to-peak photometric variability are mostly fast rotating stars (less than 13 days) and there is a hint of temperature dependency. Bottom panel in Fig. 12 shows the same 71 stars but color bar indicates the rotation period value, and circle size the $v \sin i$ obtained spectroscopically, which again confirms the previous result we found.

In Fig. 13, we present a similar plot to Fig. 12 but this time for 29 stars where we could identify faculae or spot dominated patterns using the method described in Sec. 3.2. We found 9 faculae dominated stars (which were also slow rotators as is expected for faculae dominated stars), and 20 spot-dominated stars. We show faculae and spot dominated stars in yellow and black, respectively. In this sample, 20 stars can be classified as fast rotators (rotation period < 15 days), and large fraction of them (13 out 20) are spot dominated. This result is in strong agreement with Montet et al. (2017), where they reported 15 days as the threshold in rotation period for separating spot-faculae dominated regimes. Moreover, faculae-dominated stars tend to have low photometric peak-to-peak variability, due to the low contrast of faculae’s region, and therefore are mostly below the 6.5 ppt limit. Thus, the 6.5 ppt limit can be also interpreted as the photometric variability transition between the spot-dominated and the faculae-dominated regime. However, the sample of 29 stars is too small to generalize.

6. Application of our result on the TESS planet candidates’ host stars

It is difficult to define the criteria for the most suitable targets for RV follow up of transiting planet candidates. In Sect. 4.2.1 we saw that the dependence of RV jitter on photometric peak-to-peak variation shows a hint of knee at 6.5 ppt. We use this value as an upper threshold to identify the targets on the TESS object of interest (TOI) catalog¹³ with the lowest RV jitter. We selected TOI catalog targets with publicly available light curves

¹³ <https://tess.mit.edu/toi-releases/>

in the archive. Since we are mostly interested in the cooler stars, we selected the stars with T_{eff} lower than 6800 K. Although in our sample we have filtered out the evolved stars already, we selected the stars with the radius less than $2.0 R_{\text{sun}}$ to narrow our analysis and select stars similar to our the Sun. In this sample, we used T_{eff} , R_{sun} and TESS magnitudes as reported in the TIC (Stassun et al. 2018).

We then removed all the flux points within the transit reported by the TOI catalog. After eliminating the transit light-curves, we applied the same procedures explained in the section 2.2 and estimated the peak-to-peak flux variation for each TOI host star.

In the Fig. 14, we present the results of the peak-to-peak variation versus TESS magnitude. Stars with different R_{sun} values are denoted by points with different sizes. The color denotes the effective temperature of the star. The vertical line shows where we believe a critical knee point in Fig. 9 is. The amplitude of RV jitter above this limit of photometric variability (6.5 ppt) can dramatically increase. 43 % of the stars in this sample have light curve peak-to-peak variations less than 6.5 ppt (279 out of 645 stars). Mean, median, and interquartile range of RV-RMS of the stars with photometric peak-to-peak variability below 6.5 ppt in our sample are 3.62 m s^{-1} , 2.77 m s^{-1} , and 2.54 m s^{-1} , respectively. We note that in this figure we can also clearly see a correlation between the TESS magnitude and peak-to-peak variation as well as T_{eff} , which can be part of the instrumental as well as the astrophysical effects. The correlation of the peak-to-peak light curve variation with star magnitudes can be explained by the TESS photon noise (see more Fig. 8 in Ricker et al. 2014). We tested the impact of photon noise by seeking for any correlation between the RV-RMS and stars’ magnitude, as well as between the photometric peak-to-peak variation and stars’ magnitude in our sample, and could not find any significant correlation.

7. Discussion and conclusion

We present a study on the correlation between RV jitter and photometric variability. We used a sample of 171 stars that have been observed by both the HARPS spectrograph and TESS space telescope. We derived the RV-RMS and peak-to-peak of light curve variability as well as the stellar parameters.

We found a strong correlation between the RV jitter and photometric flux variability. We divided our sample into four subsamples in order to investigate the impact of time interval between RV measurements and light curves. We found that the correlation becomes weaker as the time lags between the RV measurements and light curves increase. Within year 1 and year 2, the correlation is strong but the year 3 and year 4 show relatively weaker correlation. We can conclude the maximum time difference in which the light curve peak-to-peak

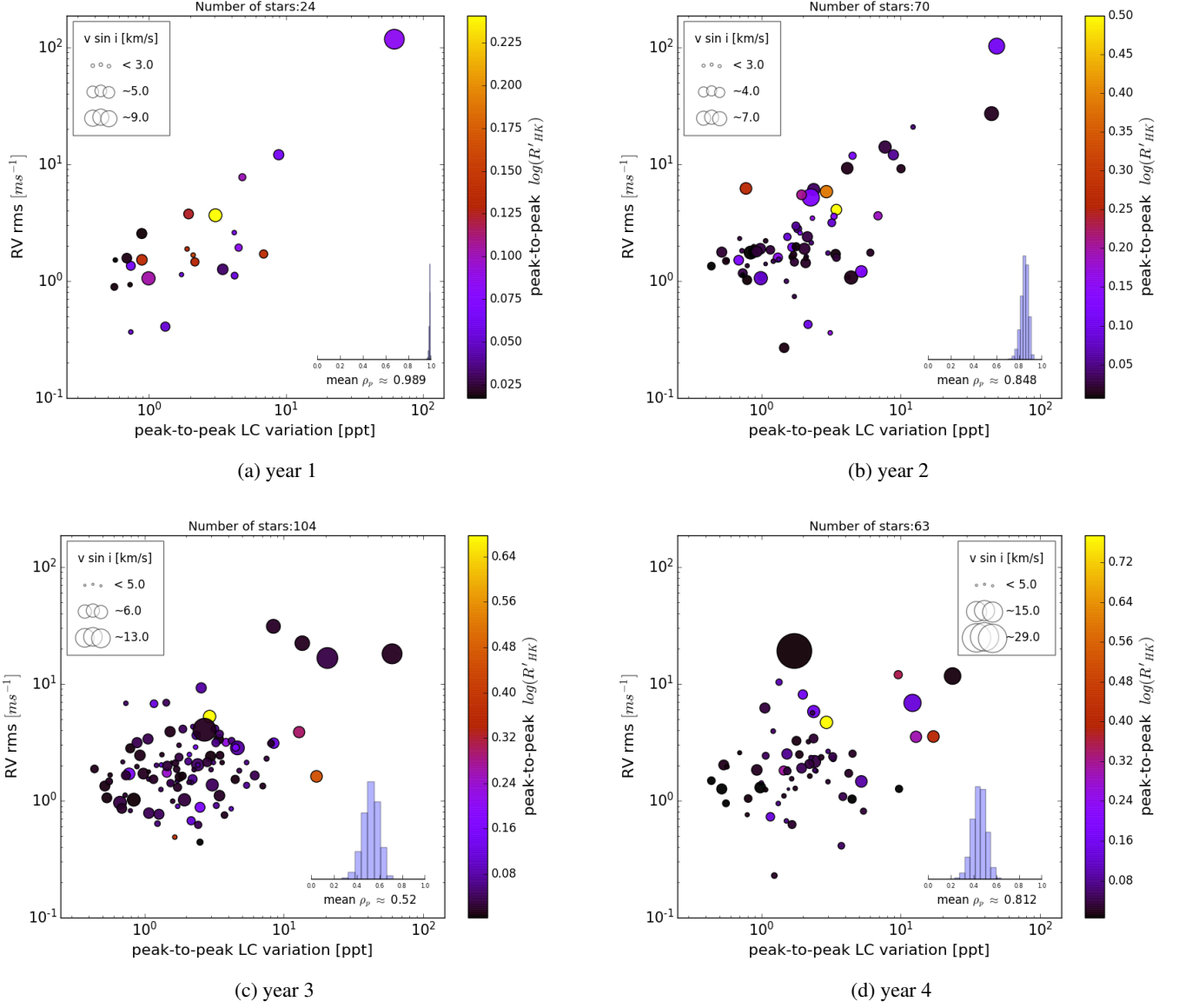


Fig. 6: RV-RMS versus photometric variability (peak-to-peak of light curve) for the year 1 (a), year 2 (b), year 3 (c) and year 4 (d) RV measurements sampling. Color bars present the peak-to-peak variation of $\log(R'_{HK})$ during the whole HARPS observations and the size-scale presents the estimation of the average $v \sin i$ derived from the CCF FWHM described in Sec. 3.1. The calculated value of correlation coefficient ρ_{sp} and its posterior distribution is presented in each panel.

can be used to predict the RV jitter is two years. After that the information content of photometric viability is lost, probably the consequence of the evolution of the stellar magnetic cycle. This could imply that majority of these stars with different spectral types should have a cycle shorter than 6 years, assuming that half an activity cycle is sufficient to bring the observables out of phase and diminishes the correlation (for instance if the RVs were taken at activity maximum and photometry were obtained at activity minimum or vice-versa).

We also examined different functional forms which could represent better the observed correlations. We compare the best fitted model using RMS_{resi} and BIC. For the whole sample the fit of piecewise power law functions, with a knee at 6.5 ppt in peak-to-peak of light curve variation, describes the data more precisely with lower RMS_{resi} without considering the cost of the two extra parameters. We also fitted the two models on the year

1, year 2, year 3, and year 4 subsampling (see Table. A.1). The results show that for the year 2, which is the closest subsampling group to the TESS observations with fairly sufficient number of data points as well as a strong correlation, the piecewise power law also describes the data better than the single power law with lower RMS_{resi} , however, the BIC is larger for the piecewise model because of the two extra parameters in this model. The correlation between RV-RMS and peak-to-peak of light curve variability of showed two regions separating with a knee point where the strength of the correlation changes. This might be due to the transition from the spot-dominated regime to the faculae-dominated regime. These two regimes have already been discussed in several studies (Lockwood et al. 1997; Radick et al. 1998; Shapiro et al. 2016; Oshagh et al. 2017; Shapiro et al. 2020)

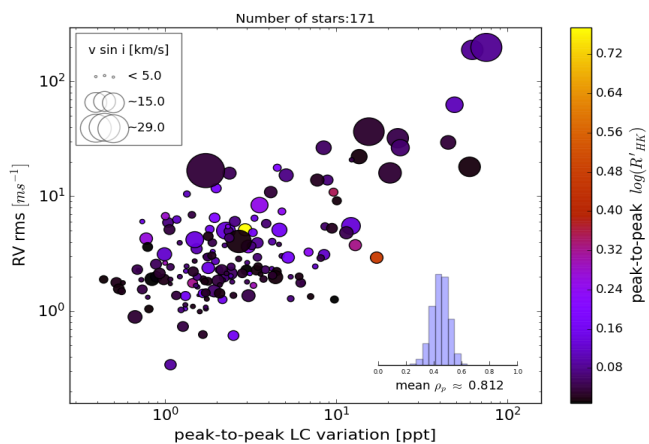


Fig. 7: Correlation between RV-RMS and peak-to-peak of light curve variation using the all years RV sampling (whole sample). Size of the points indicate the $v \sin i$ and color represent and peak-to-peak of $\log(R'_{HK})$ within the RV measurements. The points above 6 ppt have larger marker sizes and they filled up more space, thus this might cause difficulties in clearly recognizing the double law feature.

Meunier & Lagrange (2019); Meunier et al. (2019) simulated the RVs and photometric time series and derived the flux variability as well as the global RV jitter for F to early K stars. They showed that there is a relationship between the photometric variability and RV jitter considering the dependency of stellar parameters such as rotation period and T_{eff} as well as inclination. These simulations showed presence of a knee point in the correlation between photometric variability and RV jitter, however, the knee point and also the range of values are in a different domain than our findings. There could be several reason for these disagreements such as: a) our observational sample of stars could have more complex and random spot or faculae than the ones simulated in Meunier & Lagrange (2019). b) our observational RV sample were not simultaneous with the TESS light curve, while in Meunier & Lagrange (2019) the simulation were done for simultaneous observations. c) the observation sample could have unknown companions which can produce RV variation in time series. However, the dispersion of the simulations for RV-RMS and photometric variability (see Fig. 9 in Meunier & Lagrange 2019) are compatible with the observed dispersion of the whole sample.

We also found that there is a strong correlation between the chromospheric activity index ($\log(R'_{HK})$) and RV jitter and also with photometric variability, which are both in agreement with previous studies (Santos et al. 2000; Wright 2005; Saar et al. 2003; Meunier et al. 2019). Also the observed correlation between $\log(R'_{HK})$ and peak-to-peak of photometric variation is compatible to the simulation's result within the range $-5.0 < \log(R'_{HK}) < -4.6$ (see Fig. 5 in Meunier & Lagrange 2019). We provided an updated version of the relation between $\log(R'_{HK})$ and RV jitter and also with peak-to-peak of light curve variability.

We were able to estimate the rotation period of 71 stars, out of 171 stars in our sample, using the TESS light curve. Then we investigated the effect of this parameter on the correlation between RV-RMS and peak-to-peak of light curve variability. Our result demonstrated that slow rotating stars (which are the ones also we found to be faculae dominated) create lower RV jitter as

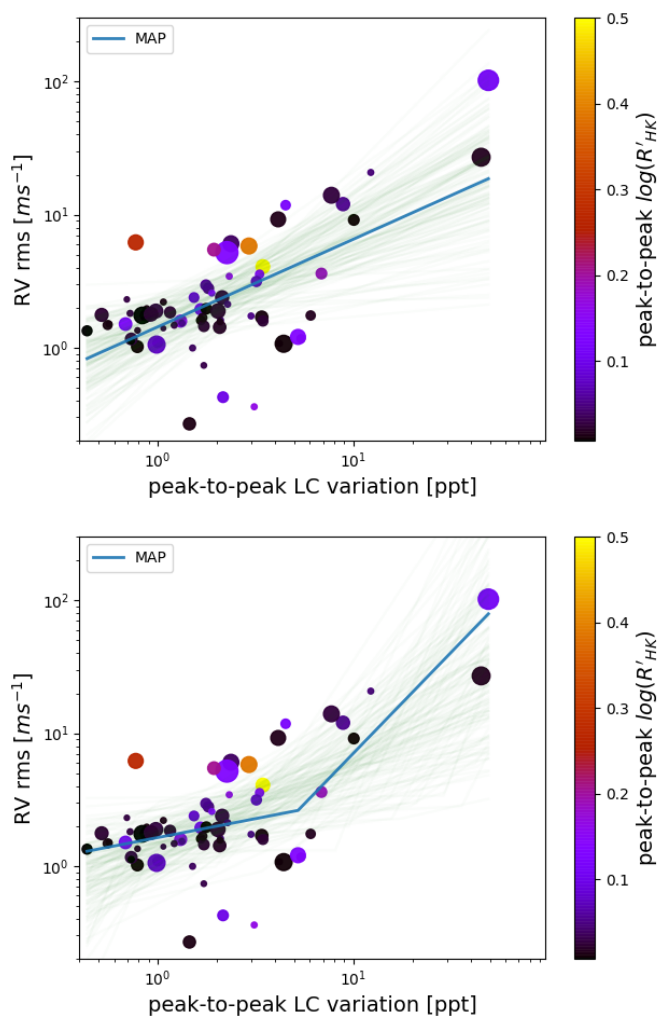


Fig. 8: Year 2 sample with single power law function fit (top plot) and a piecewise function with two power law function fit (bottom plot); In both panels the best fit indicated with the Maximum a Posteriori (MAP).

well as lower peak-to-peak photometric variability, and on the other hand fast rotating star, $P_{\text{rot}} \leq 5$ day (which are the ones also we found to be spot dominated) generate much larger RV jitter and photometric variability.

We have also looked into the correlation of the other parameters which might affect the peak-to-peak of light curve vs RV-RMS correlation such as T_{eff} , $[Fe/H]$ and the number of nights that the star has been observed in RV. We could not find any significant trend caused by these parameters on the peak-to-peak of light curve vs RV-RMS correlation (Appendix B). We also examined our results by using just the first sector for the stars which have more than one TESS sector observations and we did not see any significant changes in the results. Finally, we attempted to select the best targets, in terms of the lowest RV jitter, in TESS Objects of Interest catalog. To do that, we used our estimated knee point at 6.5 ppt in photometric variability. We estimated that 42% of the stars in a specific sample of the TOI catalog have the peak-to-peak photometric variability of less than 6.5 ppt and, therefore, will have a small amplitude RV jitter (less than $\sim 3 \text{ ms}^{-1}$) which can be essential for the confirmation of Earth-mass exoplanets at short orbits around low-mass stars in TESS objects of interest. (see Table. C.2).

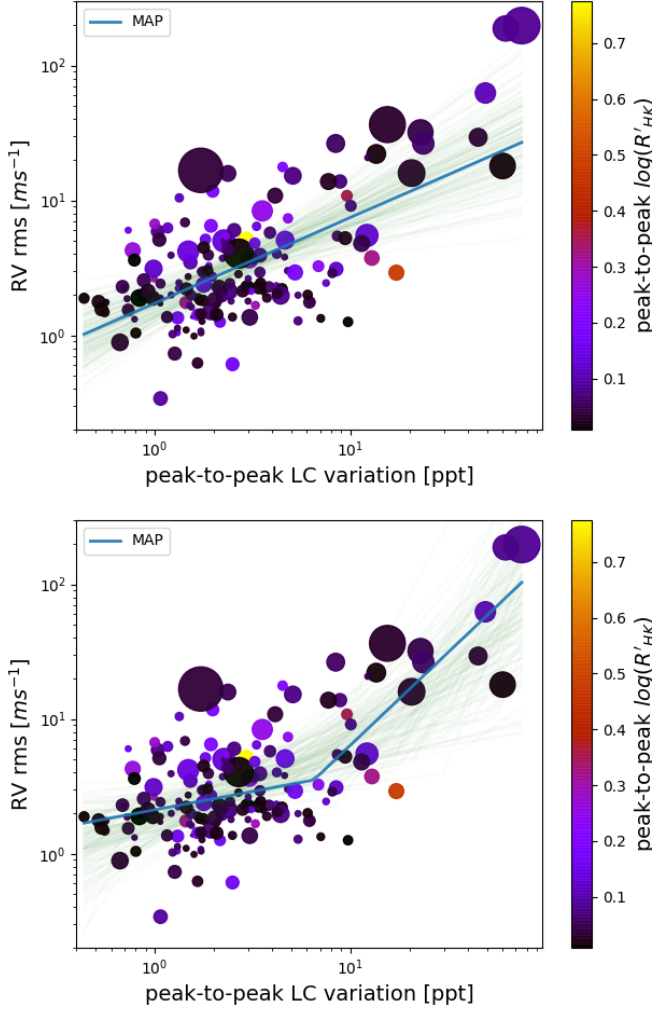


Fig. 9: Top plot: the same with single power law function fit, bottom plot: all RV sampling group with two piecewise power law fitting. In both panels the best fit indicated with the Maximum a Posteriori (MAP).

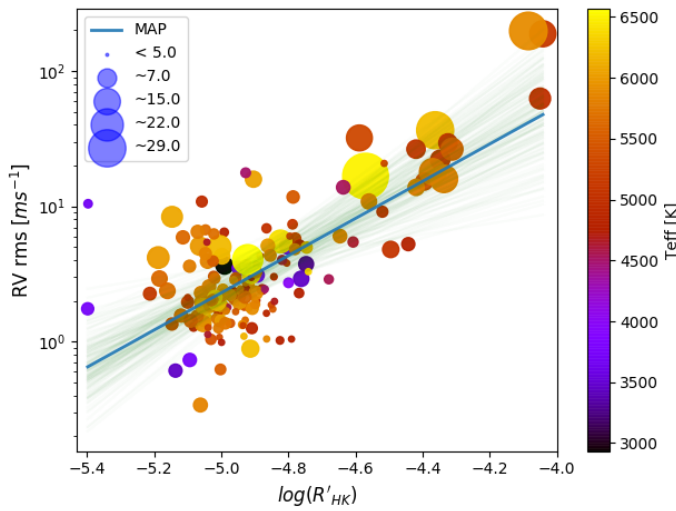


Fig. 10: $\log(R'_{HK})$ vs RV-RMS of light curve with the best fit. The same method in MCMC analysis explained in Sec.A, $\log_{10}(y) = ax + b$: $a = 1.382^{0.341}_{-0.344}$, $b = 7.271^{1.670}_{-1.683}$.

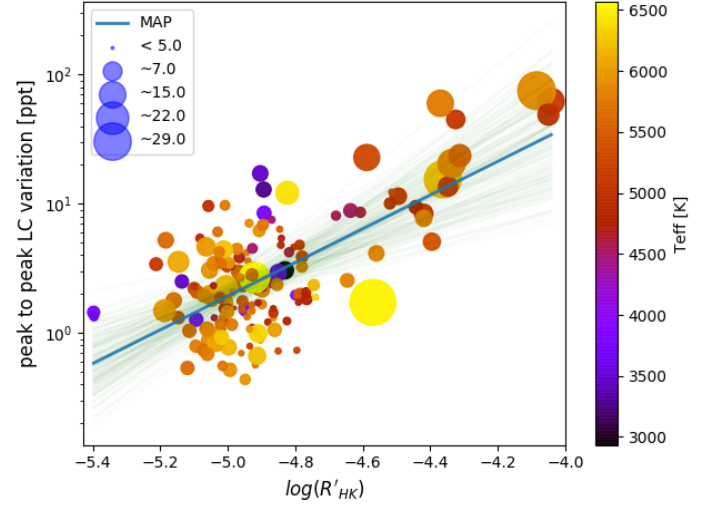


Fig. 11: $\log(R'_{HK})$ vs peak-to-peak of light curve variation with the best fit. The same method in MCMC analysis explained in Sec.A, $\log_{10}(y) = ax + b$: $a = 1.304^{0.338}_{-0.335}$, $b = 6.804^{1.659}_{-1.641}$.

Acknowledgements. We would like to thank the anonymous referee for insightful and constructive comments, which added significantly to the clarity of this paper. This work was supported by FCT - Fundação para a Ciência e a Tecnologia through national funds and by FEDER through COMPETE2020 - Programa Operacional Competitividade e Internacionalização by these grants: UID/FIS/04434/2019; UIDB/04434/2020 & UIDP/04434/2020; PTDC/FIS-AST/32113/2017 & POCI-01-0145-FEDER-032113; PTDC/FIS-AST/28953/2017 & POCI-01-0145-FEDER-028953. S.H. and B.A. acknowledge support by the fellowships PD/BD/128119/2016 and PD/BD/135226/2017 funded by FCT (Portugal) and POCH/FSE (EC). S.S., V.A., O.D.S.D. and J.P.F. acknowledge support from FCT through work contracts n^os IF/00028/2014/CP1215/CT0002, IF/00650/2015/CP1273, DL 57/2016/CP1364/CT0004, DL 57/2016/CP1364/CT0005. M.O. acknowledges the support of the Deutsche Forschungsgemeinschaft (DFG) priority program SPP 1992 ‘‘Exploring the Diversity of Extrasolar Planets (RE 1664/17-1)’’. M.O., E.A.G also acknowledge the support of the FCT/DAAD bilateral grant 2019 (DAAD ID: 57453096). M.O. acknowledges research funding from the Deutsche Forschungsgemeinschaft (DFG, German Research Foundation) - OS 508/1-1. This research made use of Astropy, a community-developed core Python package for Astronomy (Price-Whelan et al. 2018; Astropy Collaboration et al. 2013), and the NumPy, SciPy, Matplotlib, tescut, celerite Python modules (Van Der Walt et al. 2011; Jones et al. 2001–; Hunter 2007; Brasseur et al. 2019; Foreman-Mackey et al. 2017) and pandas (McKinney 2010, 2011). This research made use of Lightkurve, a Python package for Kepler and TESS data analysis (Lightkurve Collaboration et al. 2018). This paper includes data collected with the TESS mission, obtained from the MAST data archive at the Space Telescope Science Institute (STScI). Funding for the TESS mission is provided by the NASA Explorer Program. STScI is operated by the Association of Universities for Research in Astronomy, Inc., under NASA contract NAS 5–26555. This work is based on observations collected at the European Organization for Astronomical Research in the Southern Hemisphere under ESO programs: ‘0100.C-0097(A)’, ‘0100.C-0487(A)’, ‘0100.C-0836(A)’, ‘0100.D-0444(A)’, ‘0101.C-0379(A)’, ‘0101.D-0494(A)’, ‘0101.D-0494(B)’, ‘060.A-9036(A)’, ‘089.C-0732(A)’, ‘090.C-0421(A)’, ‘093.C-0062(A)’, ‘095.C-0040(A)’, ‘095.C-0551(A)’, ‘095.C-0799’, ‘095.C-0799(A)’, ‘096.C-0053(A)’, ‘096.C-0460(A)’, ‘096.C-0499(A)’, ‘096.C-0876(A)’, ‘097.C-0021(A)’, ‘097.C-0090(A)’, ‘097.C-0390(B)’, ‘097.C-0571(A)’, ‘098.C-0518(A)’, ‘098.C-0269(A)’, ‘098.C-0269(B)’, ‘098.C-0366(A)’, ‘098.C-0518(A)’, ‘098.C-0739(A)’, ‘099.C-0205(A)’, ‘099.C-0458(A)’, ‘099.C-0798(A)’, ‘183.C-0437(A)’, ‘188.C-0265(O)’, ‘188.C-0265(P)’, ‘188.C-0265(Q)’, ‘188.C-0265(R)’, ‘190.C-0027(A)’, ‘191.C-0873(A)’, ‘192.C-0224’, ‘192.C-0224(C)’, ‘192.C-0852(A)’, ‘196.C-0042’, ‘196.C-0042(D)’, ‘196.C-0042(E)’, ‘196.C-1006(A)’, ‘198.C-0836(A)’, ‘198.C-0838(A)’, ‘60.A-9036(A)’, ‘Lagrange’.

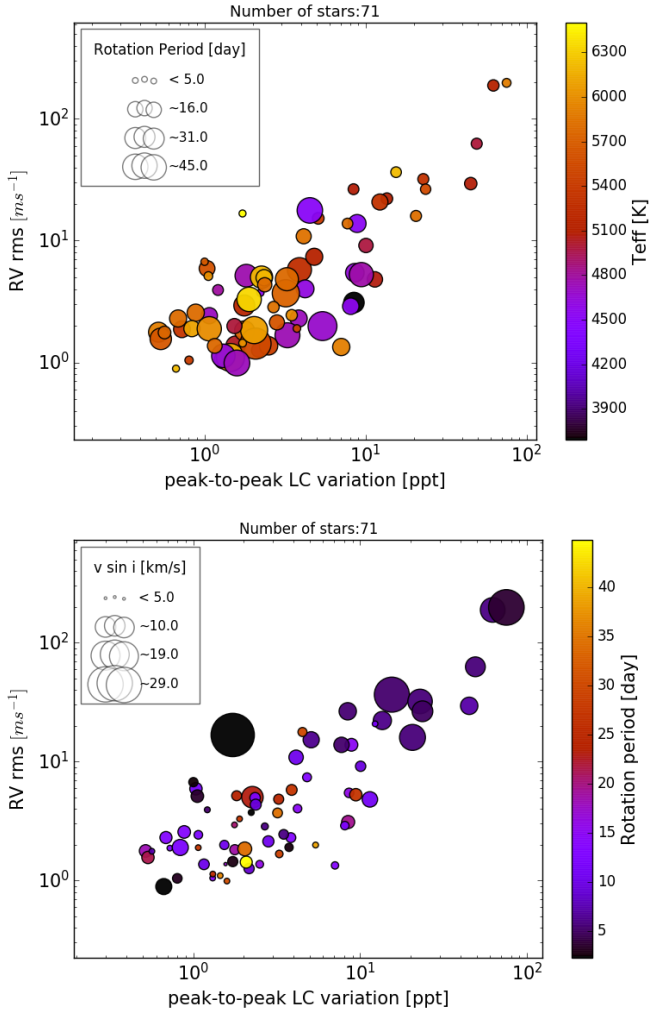


Fig. 12: RV-RMS and peak-to-peak of light curve variation for the subsample of 71 stars. Top plot: Circle sizes represents the value of rotation period found by GPS method, see Table. C.1. Color bar indicates the stellar effective temperature. Bottom plot: Similar than top panel but, color bar indicates the rotation period value, and circle size the $v \sin i$ obtained spectroscopically

References

- Adibekyan, V., Sousa, S. G., & Santos, N. C. 2018, in *Asteroseismology and Exoplanets: Listening to the Stars and Searching for New Worlds*, ed. T. L. Campante, N. C. Santos, & M. J. P. F. G. Monteiro, Vol. 49, 225
- Aigrain, S., Pont, F., & Zucker, S. 2012, *MNRAS*, 419, 3147
- Amazo-Gomez, E.M., Shapiro, A.I., Solanki, S.K., et al. 2020, *A&A*, submitted
- Amazo-Gómez, E. M., Shapiro, A. I., Solanki, S. K., et al. 2020, Rotation periods from the inflection point in the power spectrum of stellar brightness variations: II. The Sun
- Arevalo, F., Cid, A., & Moya, J. 2017, *European Physical Journal C*, 77, 565
- Astropy Collaboration, Robitaille, T. P., Tollerud, E. J., et al. 2013, *A&A*, 558, A33
- Barros, S. C. C., Almenara, J. M., Deleuil, M., et al. 2014, *A&A*, 569, A74
- Bastien, F. A., Stassun, K. G., Basri, G., & Pepper, J. 2013, *Nature*, 500, 427
- Bastien, F. A., Stassun, K. G., Pepper, J., et al. 2014, *AJ*, 147, 29
- Boisse, I., Bouchy, F., Hébrard, G., et al. 2011, in *IAU Symposium*, Vol. 273, *Physics of Sun and Star Spots*, ed. D. Prasad Choudhary & K. G. Strassmeier, 281–285
- Boisse, I., Bouchy, F., Hébrard, G., et al. 2011, *A&A*, 528, A4
- Borucki, W. J., Koch, D., Basri, G., et al. 2010, *Science*, 327, 977
- Brasseur, C. E., Phillip, C., Fleming, S. W., Mullally, S. E., & White, R. L. 2019, *Astrocut: Tools for creating cutouts of TESS images*
- Bryson, S. T., Jenkins, J. M., Klaus, T. C., et al. 2017, *Kepler Data Processing Handbook: Target and Aperture Definitions: Selecting Pixels for Kepler Downlink*, Tech. rep.

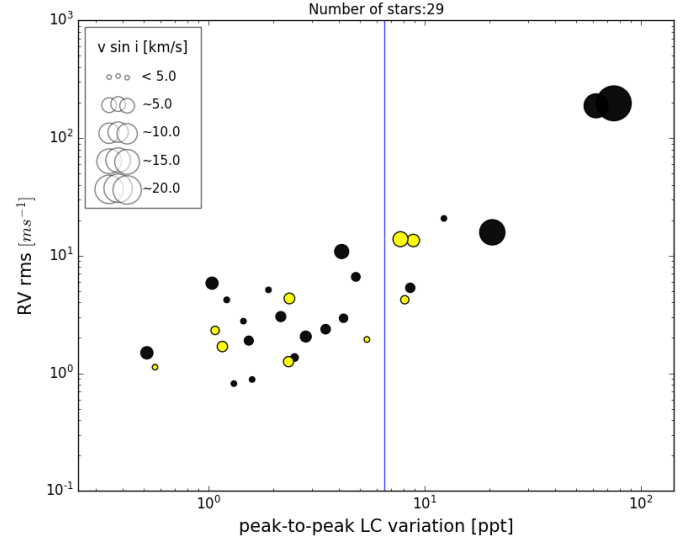


Fig. 13: RV-RMS and the peak-to-peak of light curve variation for the subsample of 20 stars with spot dominance and 9 stars with faculae dominance in their light curves. Circle sizes represents the $v \sin i$ value determined spectroscopically. Black color indicates spot dominated and yellow indicates faculae dominated. The Blue vertical line shows the knee point presented in Fig. 9 in peak-to-peak light curve variation at 6.5 ppt.

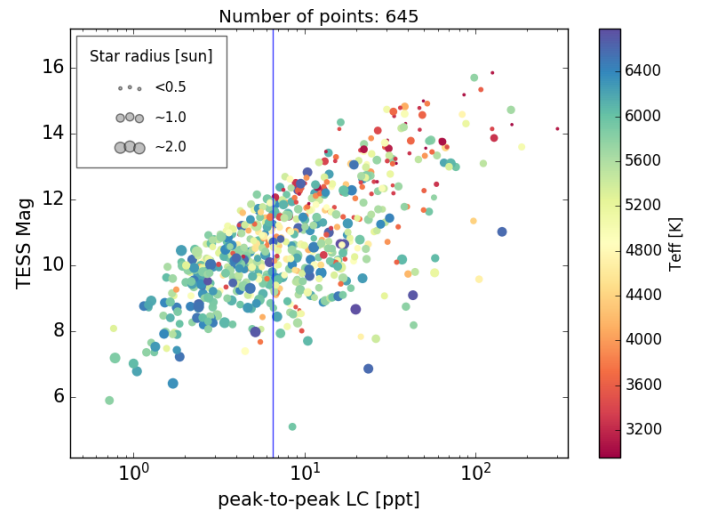


Fig. 14: Peak-to-peak of light curve versus TESS mag. Color bar shows the stellar effective temperature and size shows the stellar radius. The Blue vertical line shows the knee point presented in Fig. 9 in peak-to-peak light curve variation at 6.5 ppt.

- Cegla, H. M., Stassun, K. G., Watson, C. A., Bastien, F. A., & Pepper, J. 2014, *ApJ*, 780, 104
- Cloutier, R., Doyon, R., Bouchy, F., & Hébrard, G. 2018, *AJ*, 156, 82
- Czesla, S., Huber, K. F., Wolter, U., Schröter, S., & Schmitt, J. H. M. M. 2009, *A&A*, 505, 1277
- Desort, M., Lagrange, A. M., Galland, F., Udry, S., & Mayor, M. 2007, *A&A*, 473, 983
- Díaz, R. F., Ségransan, D., Udry, S., et al. 2016, *A&A*, 585, A134
- Dumusque, X., Santos, N. C., Udry, S., Lovis, C., & Bonfils, X. 2011a, *A&A*, 527, A82
- Dumusque, X., Udry, S., Lovis, C., Santos, N. C., & Monteiro, M. J. P. F. G. 2011b, *A&A*, 525, A140
- Duncan, D. K., Vaughan, A. H., Wilson, O. C., et al. 1991, *ApJS*, 76, 383

- Figueira, P., Faria, J. P., Adibekyan, V. Z., Oshagh, M., & Santos, N. C. 2016, *Origins of Life and Evolution of the Biosphere*, 46, 385
- Figueira, P., Marmier, M., Bonfils, X., et al. 2010, *A&A*, 513, L8
- Findeisen, K., Hillenbrand, L., & Soderblom, D. 2011, *AJ*, 142, 23
- Fischer, D. A., Anglada-Escude, G., Arriagada, P., et al. 2016, *PASP*, 128, 066001
- Fischer, D. A. & Valenti, J. 2005, *The Astrophysical Journal*, 622, 1102
- Foreman-Mackey, D., Agol, E., Angus, R., & Ambikasaran, S. 2017, *ArXiv*
- Foreman-Mackey, D., Hogg, D. W., Lang, D., & Goodman, J. 2013, *PASP*, 125, 306
- Gomes da Silva, J., Figueira, P., Santos, N., & Faria, J. 2018, *The Journal of Open Source Software*, 3, 667
- Gomes da Silva, J., Santos, N. C., Bonfils, X., et al. 2011, *A&A*, 534, A30
- Hojjatpanah, S., Figueira, P., Santos, N. C., et al. 2019, *A&A*, 629, A80
- Huélamo, N., Figueira, P., Bonfils, X., et al. 2008, *A&A*, 489, L9
- Hunter, J. D. 2007, *Computing in Science & Engineering*, 9, 9
- Jones, E., Oliphant, T., Peterson, P., et al. 2001–, *SciPy: Open source scientific tools for Python*, [Online; accessed <today>]
- Korhonen, H., Andersen, J. M., Piskunov, N., et al. 2015, *MNRAS*, 448, 3038
- Liddle, A. R. 2007, *MNRAS*, 377, L74
- Lightkurve Collaboration, Cardoso, J. V. d. M., Hedges, C., et al. 2018, *Lightkurve: Kepler and TESS time series analysis in Python*, *Astrophysics Source Code Library*
- Lo Curto, G., Pepe, F., Avila, G., et al. 2015, *The Messenger*, 162, 9
- Lockwood, G. W., Skiff, B. A., & Radick, R. R. 1997, *ApJ*, 485, 789
- Maldonado, J., Scandariato, G., Stelzer, B., et al. 2017, *Astronomy & Astrophysics*, 598, A27
- Mamajek, E. E. & Hillenbrand, L. A. 2008, *ApJ*, 687, 1264
- Martin, D. C., Fanson, J., Schiminovich, D., et al. 2005, *ApJ*, 619, L1
- Mayor, M., Pepe, F., Queloz, D., et al. 2003, *The Messenger*, 114, 20
- Mayor, M., Udry, S., Naef, D., et al. 2004, *Astronomy & Astrophysics*, 415, 391
- McKinney, W. 2010, in *Proceedings of the 9th Python in Science Conference*, Vol. 445, Austin, TX, 51–56
- McKinney, W. 2011, *Python for High Performance and Scientific Computing*, 14
- Meunier, N. & Lagrange, A. M. 2019, *A&A*, 629, A42
- Meunier, N., Lagrange, A. M., & Cuzacq, S. 2019, *A&A*, 632, A81
- Montet, B. T., Tovar, G., & Foreman-Mackey, D. 2017, *ApJ*, 851, 116
- Morris, R. L., Twicken, J. D., Smith, J. C., et al. 2017, *Kepler Data Processing Handbook: Photometric Analysis*, Tech. rep.
- Neves, V., Bonfils, X., Santos, N., et al. 2014, *Astronomy & Astrophysics*, 568, A121
- Nielsen, M. B., Gizon, L., Schunker, H., & Karoff, C. 2013, *A&A*, 557, L10
- Noyes, R. W., Hartmann, L. W., Baliunas, S. L., Duncan, D. K., & Vaughan, A. H. 1984, *ApJ*, 279, 763
- Oshagh, M. 2018, in *Asteroseismology and Exoplanets: Listening to the Stars and Searching for New Worlds*, Vol. 49, 239
- Oshagh, M., Boisse, I., Boué, G., et al. 2013a, *A&A*, 549, A35
- Oshagh, M., Santos, N. C., Boisse, I., et al. 2015, in *European Physical Journal Web of Conferences*, Vol. 101, 05003
- Oshagh, M., Santos, N. C., Boisse, I., et al. 2013b, *A&A*, 556, A19
- Oshagh, M., Santos, N. C., Figueira, P., et al. 2017, *A&A*, 606, A107
- Pepe, F., Molaro, P., Cristiani, S., et al. 2014, *Astronomische Nachrichten*, 335, 8
- Price-Whelan, A. M., Sipőcz, B. M., Günther, H. M., et al. 2018, *AJ*, 156, 123
- Queloz, D., Henry, G. W., Sivan, J. P., et al. 2001, *A&A*, 379, 279
- Radick, R. R., Lockwood, G. W., Skiff, B. A., & Baliunas, S. L. 1998, *ApJS*, 118, 239
- Rauer, H., Catala, C., Aerts, C., et al. 2014, *Experimental Astronomy*, 38, 249
- Reffert, S., Bergmann, C., Quirrenbach, A., Trifonov, T., & Künstler, A. 2015, *Astronomy & Astrophysics*, 574, A116
- Reinhold, T. & Hekker, S. 2020, *arXiv e-prints*, arXiv:2001.08214
- Ricker, G. R., Winn, J. N., Vanderspek, R., et al. 2014, in *Society of Photo-Optical Instrumentation Engineers (SPIE) Conference Series*, Vol. 9143, Proc. SPIE, 914320
- Ricker, G. R., Winn, J. N., Vanderspek, R., et al. 2014, *Journal of Astronomical Telescopes, Instruments, and Systems*, 1, 014003
- Robertson, P., Mahadevan, S., Endl, M., & Roy, A. 2014, *Science*, 345, 440
- Saar, S. H., Butler, R. P., & Marcy, G. W. 1998, *ApJ*, 498, L153
- Saar, S. H. & Donahue, R. A. 1997, *ApJ*, 485, 319
- Saar, S. H., Hatzes, A., Cochran, W., & Paulson, D. 2003, in *Cambridge Workshop on Cool Stars, Stellar Systems, and the Sun*, Vol. 12, *The Future of Cool-Star Astrophysics: 12th Cambridge Workshop on Cool Stars, Stellar Systems, and the Sun*, ed. A. Brown, G. M. Harper, & T. R. Ayres, 694–698
- Santos, N. C., Gomes da Silva, J., Lovis, C., & Melo, C. 2010, *A&A*, 511, A54
- Santos, N. C., Mayor, M., Naef, D., et al. 2000, *A&A*, 361, 265
- Santos, N. C., Mayor, M., Naef, D., et al. 2002, *A&A*, 392, 215
- Santos, N. C., Mortier, A., Faria, J. P., et al. 2014, *A&A*, 566, A35
- Shapiro, A. I., Amazo-Gómez, E. M., Krivova, N. A., & Solanki, S. K. 2020, *A&A*, 633, A32
- Shapiro, A. I., Solanki, S. K., Krivova, N. A., Yeo, K. L., & Schmutz, W. K. 2016, *A&A*, 589, A46
- Shapiro, A. I., Amazo-Gómez, E. M., Krivova, N. A., & Solanki, S. K. 2020, *A&A*, 633, A32
- Sousa, S. G. 2014, [arXiv:1407.5817] [arXiv:1407.5817]
- Stassun, K. G., Oelkers, R. J., Pepper, J., et al. 2018, *AJ*, 156, 102
- Tayar, J., Stassun, K. G., & Corsaro, E. 2019, *ApJ*, 883, 195
- Van Der Walt, S., Colbert, S. C., & Varoquaux, G. 2011, *Computing in Science & Engineering*, 13, 22
- Vaughan, A. H., Preston, G. W., & Wilson, O. C. 1978, *PASP*, 90, 267
- Vida, K., Oláh, K., Kóvári, Z., et al. 2019, *ApJ*, 884, 160
- Wright, J. T. 2005, *PASP*, 117, 657

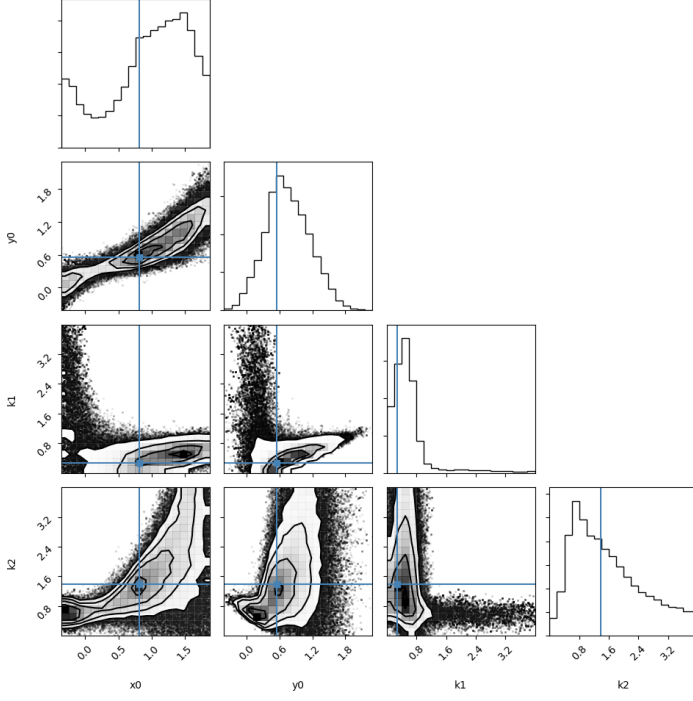


Fig. B.1: Posterior distribution for parameters x_0 , y_0 , k_1 , k_2 in Eq. A.1

Appendix A: Correlation and uncertainties estimation

We compare the piecewise two power law function fit and single power law function fit in the peak-to-peak of photometric variability and RV jitter correlation plot. We used Markov-chain Monte Carlo (MCMC) sampling using the library *emcee* (Foreman-Mackey et al. 2013) to estimate the uncertainties of the parameters in both models.

For the piecewise function we used

$$\log_{10}(y) = \begin{cases} k_1 \log_{10}(x) + y_0 - k_1 x_0 & \log(x) < x_0 \\ k_2 \log_{10}(x) + y_0 - k_2 x_0 & \log(x) \geq x_0 \end{cases} \quad (\text{A.1})$$

which here $(10^{x_0}, 10^{y_0})$ is the knee point coordination in the plots. We also fit a single power law function fit as,

$$\log_{10}(y) = a \log_{10}(x) + b. \quad (\text{A.2})$$

We derived RMS_{resi} and BIC value in order to compare the significance of the two models. All best fitted parameters are presented in Table. A.1.

Appendix B: Correlation with other observable

By having the effective temperature estimated, we investigated the correlation between T_{eff} and RV-RMS versus peak-to-peak photometric variability. In Fig. B.3, we used T_{eff} for the color bar. We cannot confirm a significant dependency of the plots on T_{eff} .

We also inspected if the correlation between RV and photometric jitter has any dependency on the $[Fe/H]$, and also the number of nights that the star has been observed in RV (see in Fig. B.4). We did not find significant correlation between these parameters.

Appendix C: Table: stellar parameters

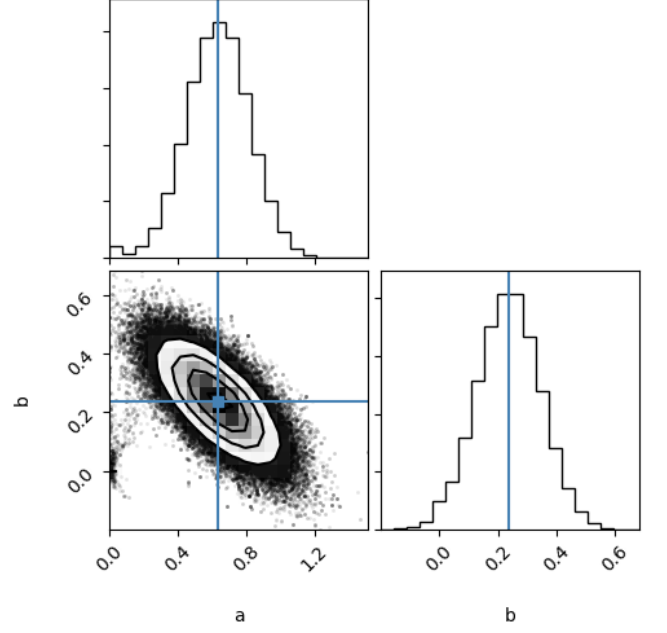


Fig. B.2: Posterior distribution for parameters a, b in Eq. A.2

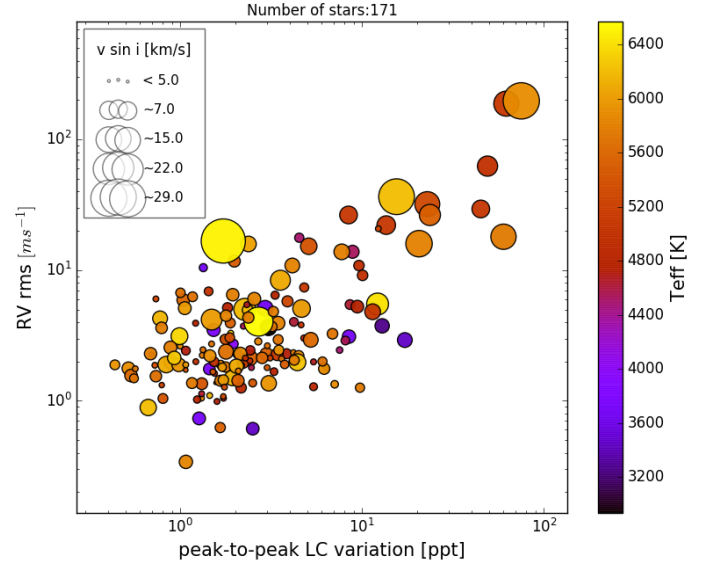


Fig. B.3: Same plots as Fig. 7 with color bar T_{eff}

	Single		Posterior				RMS_{resi}		BIC	
	a	b	x_0	y_0	k_1	k_2	Single	Piecewise	Single	Piecewise
year 1	0.825 ^{0.417} _{-0.399}	0.038 ^{0.233} _{-0.225}	0.610 ^{0.573} _{-0.788}	0.338 ^{0.664} _{-0.470}	0.392 ^{0.635} _{-0.458}	1.450 ^{1.396} _{-0.833}	0.30	0.25	8.6	14.3
year 2	0.659 ^{0.289} _{-0.285}	0.156 ^{0.144} _{-0.148}	0.718 ^{0.570} _{-0.875}	0.419 ^{0.514} _{-0.384}	0.285 ^{0.337} _{-0.347}	1.523 ^{1.427} _{-0.690}	0.32	0.28	15.7	22.7
year 3	0.374 ^{0.249} _{-0.222}	0.185 ^{0.120} _{-0.126}	0.733 ^{0.527} _{-1.031}	0.343 ^{0.367} _{-0.262}	0.159 ^{0.420} _{-0.252}	1.004 ^{1.554} _{-0.647}	0.29	0.27	18.1	26.6
year 4	0.304 ^{0.307} _{-0.241}	0.214 ^{0.148} _{-0.154}	0.733 ^{0.473} _{-0.864}	0.320 ^{0.298} _{-0.255}	0.100 ^{0.983} _{-0.328}	0.939 ^{1.621} _{-0.522}	0.33	0.32	15.3	23.1
Whole sample	0.636 ^{0.179} _{-0.183}	0.238 ^{0.107} _{-0.108}	0.813 ^{0.484} _{-0.792}	0.548 ^{0.437} _{-0.366}	0.273 ^{0.306} _{-0.268}	1.381 ^{1.305} _{-0.735}	0.35	0.29	28.3	35.7

Table A.1: Maximum a Posteriori (MAP) with error for parameters which described in the Eq. A.1 and Eq. A.2 as well as the Bayesian information criterion (BIC) and RMS of the residual (RMS_{resi}) between the model and data for the two models: single power law function and piecewise power laws functions. Prior for b, x_0 and y_0 is a uniform prior with lower and upper limits (e.g., : for x_0 : $\mathcal{U}(\min(x), \max(x))$) and for a, k_1 and k_2 is $\mathcal{U}(0, 4)$.

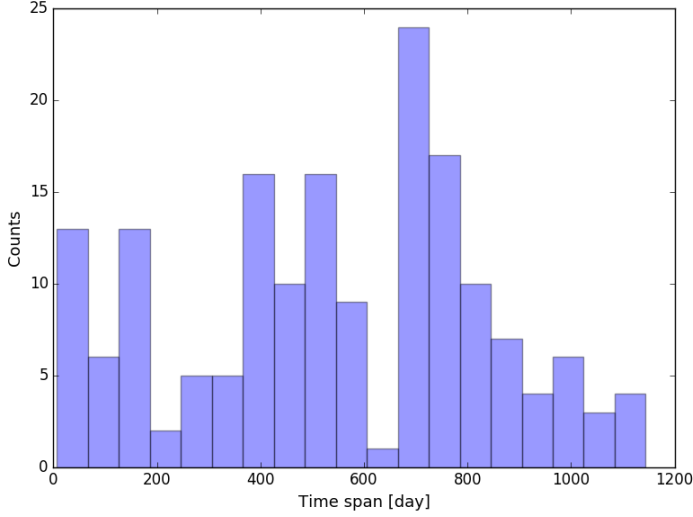


Fig. B.4: Time spans histogram of RV measurements in the sample.

Table C.1: Derived parameters for the stars

Index	Star	T_{eff} [K]	RV-RMS ¹ [$m s^{-1}$]	pp Light curves [ppt]	$v \sin i$ ² [$km s^{-1}$]	mean($\log(R'_{HK})$) ³	$\log g$ [$cm s^{-2}$]	[Fe/H]	P_{rot} [day]	Sample ⁴
1	GJ1061	2934.0 ± 90	3.65	3.055	4.0	-4.74	–	-0.08 ± 0.05	–	1
2	GJ180	3662.0 ± 90	10.456	1.339	1.0	-5.4	–	-0.24 ± 0.05	–	4
3	GJ3135	3649.0 ± 90	5.105	2.931	3.7	-4.95	–	-0.34 ± 0.05	–	2,3,4
4	GJ3440	3693.0 ± 90	3.101	8.47	2.7	-4.89	–	–	19.5 ± 1.2	3
5	GJ588	3459.0 ± 90	0.612	2.503	2.4	-5.14	–	0.06 ± 0.05	–	3
6	Gl213	3266.0 ± 90	3.748	12.893	3.1	-4.94	–	-0.16 ± 0.05	–	3,4
7	Gl229	3785.0 ± 90	3.488	1.525	2.6	-4.95	–	-0.02 ± 0.05	–	3,4
8	Gl693	3457.0 ± 90	2.919	17.185	3.3	-4.86	–	-0.275 ± 0.05	–	3,4
9	Gl87	3726.0 ± 90	1.752	1.445	2.0	-5.4	–	-0.35 ± 0.05	–	3,4
10	HD 149189	3726.0 ± 90	0.733	1.269	2.4	-5.09	–	0.19 ± 0.05	–	3
11	HD000105	6221.0 ± 94	36.513	15.471	19.1	-4.36	4.71 ± 0.09	-0.13 ± 0.068	5.3 ± 1.9	w
12	HD007661	5410.0 ± 30	15.244	5.088	4.1	-4.4	4.38 ± 0.05	-0.01 ± 0.022	6.3 ± 1.1	w
13	HD017925	5086.0 ± 41	29.416	44.961	4.7	-4.32	4.29 ± 0.09	0.075 ± 0.023	7.2 ± 2.6	2
14	HD018599	5077.0 ± 38	26.463	8.423	4.7	-4.42	4.34 ± 0.08	-0.01 ± 0.022	5.4 ± 0.7	3
15	HD021175	5263.0 ± 39	5.773	3.889	1.8	-4.78	4.33 ± 0.07	0.12 ± 0.026	27.1 ± 2.3	w
16	HD024916	4644.0 ± 97	5.454	8.58	1.4	-4.61	4.14 ± 0.36	-0.097 ± 0.042	16.0 ± 3.9	w
17	HD037572	5314.0 ± 36	32.029	22.83	9.3	-4.59	4.4 ± 0.07	-0.344 ± 0.023	5.6 ± 3.0	w
18	HD092945	5091.0 ± 38	22.13	13.576	5.1	-4.35	4.39 ± 0.08	-0.04 ± 0.022	6.2 ± 11.1	3
19	HD102438	5547.0 ± 12	2.277	2.98	2.5	-4.97	4.42 ± 0.03	-0.29 ± 0.01	–	3
20	HD10360	5026.0 ± 31	3.808	4.619	0.5	-4.8	4.37 ± 0.07	-0.205 ± 0.017	–	3
21	HD103743	5763.0 ± 33	18.031	59.935	9.5	-4.37	4.55 ± 0.04	-0.02 ± 0.025	–	3
22	HD103891	6053.0 ± 20	15.874	2.373	3.6	-4.9	3.99 ± 0.03	-0.2 ± 0.016	–	24
23	HD107094	5522.0 ± 27	1.742	6.351	0.5	-4.85	4.43 ± 0.03	-0.51 ± 0.021	–	w
24	HD109200	5040.0 ± 30	1.373	1.562	0.2	-4.98	4.27 ± 0.07	-0.285 ± 0.018	17.4 ± 0.7	3,4
25	HD111777	5622.0 ± 22	1.446	1.649	0.5	-4.93	4.37 ± 0.04	-0.7 ± 0.018	–	3,4
26	HD114853	5668.0 ± 13	2.262	0.698	0.4	-4.96	4.36 ± 0.02	-0.23 ± 0.01	–	2,3,4
27	HD11507	3991.0 ± 90	2.725	1.965	1.3	-4.8	–	-0.21 ± 0.05	–	w
28	HD11608	4864.0 ± 106	1.259	2.161	1.6	-4.91	4.08 ± 0.23	0.22 ± 0.057	8.8 ± 2.1	1,2,3
29	HD118466	4967.0 ± 72	10.849	9.613	1.6	-5.06	4.1 ± 0.19	0.2 ± 0.038	–	4
30	HD118563	5502.0 ± 22	11.73	1.984	2.1	-4.79	4.39 ± 0.05	-0.04 ± 0.017	–	4
31	HD121004	5672.0 ± 27	2.639	3.012	0.5	-4.93	4.39 ± 0.03	-0.71 ± 0.021	–	4
32	HD123651	5877.0 ± 27	1.048	1.308	0.5	-4.86	4.4 ± 0.03	-0.48 ± 0.022	14.7 ± 4.9	w
33	HD125072	4731.0 ± 126	2.293	3.845	1.5	-4.97	3.95 ± 0.3	0.23 ± 0.058	13.6 ± 2.8	3,4
34	HD126803	5455.0 ± 19	1.794	3.005	0.5	-4.93	4.42 ± 0.04	-0.63 ± 0.016	–	2,3,4
35	HD128571	6156.0 ± 32	1.098	1.451	0.5	-4.93	4.26 ± 0.04	-0.37 ± 0.021	36.3 ± 6.5	4
36	HD129642	4851.0 ± 46	1.282	5.408	0.9	-5.08	4.18 ± 0.14	-0.09 ± 0.026	–	2,3,4
37	HD133633	5557.0 ± 24	2.128	2.409	3.6	-4.95	4.38 ± 0.03	-0.45 ± 0.019	–	3,4
38	HD134606	5619.0 ± 30	5.906	1.039	2.4	-5.11	4.28 ± 0.07	0.27 ± 0.023	11.6 ± 2.0	w
39	HD137676	5249.0 ± 16	1.961	2.212	2.0	-5.1	3.88 ± 0.04	-0.53 ± 0.013	–	3,4
40	HD13808	5034.0 ± 36	6.884	1.432	1.1	-4.87	4.34 ± 0.08	-0.2 ± 0.02	–	3
41	HD1388	5920.0 ± 13	1.772	0.519	2.4	-4.99	4.33 ± 0.02	-0.01 ± 0.011	18.3 ± 2.6	2,3,4
42	HD141624	5887.0 ± 18	2.14	2.27	0.5	-4.94	4.4 ± 0.04	-0.38 ± 0.014	–	3,4
43	HD142709	4573.0 ± 132	1.795	2.463	0.5	-4.98	4.44 ± 0.34	-0.32 ± 0.031	–	4
44	HD14412	5344.0 ± 21	1.871	0.725	0.5	-4.85	4.42 ± 0.05	-0.47 ± 0.017	13.0 ± 0.3	1,2,3
45	HD144628	4979.0 ± 42	2.021	2.416	0.5	-4.89	4.34 ± 0.08	-0.36 ± 0.024	–	3,4
46	HD14745	6182.0 ± 27	4.274	0.774	3.3	-5.0	4.42 ± 0.02	-0.14 ± 0.019	–	2,3
47	HD150139	5904.0 ± 26	2.62	0.999	0.5	-4.91	4.16 ± 0.03	-0.51 ± 0.02	–	4
48	HD150474	5423.0 ± 18	1.352	1.313	2.1	-5.15	3.93 ± 0.03	0.01 ± 0.015	–	1,2
49	HD154577	4868.0 ± 36	1.623	1.543	0.5	-4.87	4.44 ± 0.09	-0.65 ± 0.018	–	3,4
50	HD156098	6418.0 ± 37	5.506	12.165	7.2	-4.82	3.86 ± 0.05	0.12 ± 0.026	–	4
51	HD1581	5946.0 ± 17	1.885	0.437	1.4	-4.95	4.44 ± 0.03	-0.2 ± 0.013	–	2,3,4
52	HD16280	4625.0 ± 168	4.02	4.216	1.1	-4.82	4.22 ± 0.41	-0.19 ± 0.103	14.8 ± 3.9	13
53	HD16548	5685.0 ± 15	2.377	1.785	3.3	-5.16	3.95 ± 0.04	0.15 ± 0.012	–	w
54	HD16905	4760.0 ± 104	5.159	1.821	1.5	-4.77	4.14 ± 0.27	0.15 ± 0.06	23.8 ± 0.2	2
55	HD172568	5690.0 ± 18	1.865	2.176	0.5	-4.93	4.41 ± 0.03	-0.37 ± 0.014	–	3,4
56	HD17970	5005.0 ± 30	1.994	1.218	0.5	-5.0	4.34 ± 0.08	-0.45 ± 0.019	–	2,3
57	HD181327	6502.0 ± 90	16.722	1.724	29.1	-4.57	–	0.055 ± 0.05	2.3 ± 4.6	4
58	HD183414	5816.0 ± 33	15.956	20.565	10.4	-4.34	4.51 ± 0.04	-0.165 ± 0.026	5.6 ± 1.0	3
59	HD183783	4796.0 ± 77	3.93	1.215	0.5	-4.88	4.14 ± 0.47	-0.21 ± 0.031	5.4 ± 2.2	4
60	HD185283	4754.0 ± 65	1.671	3.277	0.9	-5.01	4.24 ± 0.16	-0.06 ± 0.03	28.9 ± 0.6	3,4
61	HD187456	4715.0 ± 90	2.42	1.073	1.2	-4.93	4.09 ± 0.24	0.02 ± 0.054	12.1 ± 1.6	4
62	HD189567	5710.0 ± 12	2.726	1.486	0.5	-4.93	4.37 ± 0.02	-0.24 ± 0.01	–	w
63	HD190248	5653.0 ± 77	1.561	0.536	2.4	-5.12	4.6 ± 0.13	0.33 ± 0.056	21.4 ± 9.3	3,4
64	HD19230	5118.0 ± 31	7.372	4.805	1.2	-4.79	4.37 ± 0.06	-0.57 ± 0.021	13.5 ± 4.1	1
65	HD19641	5811.0 ± 12	1.426	1.659	1.8	-5.01	4.38 ± 0.03	-0.01 ± 0.01	–	2
66	HD197481	5129.0 ± 262	188.286	62.137	9.4	-4.04	4.36 ± 0.5	0.1 ± 0.172	6.0 ± 1.1	1
67	HD199288	5756.0 ± 17	1.76	0.566	0.5	-4.92	4.47 ± 0.03	-0.63 ± 0.014	7.5 ± 1.3	1,2,3,4
68	HD199604	5785.0 ± 34	2.338	4.192	0.5	-4.94	4.27 ± 0.03	-0.62 ± 0.027	–	1,2,3
69	HD199847	5722.0 ± 27	2.23	1.321	0.5	-5.02	4.14 ± 0.03	-0.54 ± 0.021	–	3,4
70	HD199981	4559.0 ± 149	2.893	8.093	1.1	-4.68	4.3 ± 0.55	-0.16 ± 0.05	12.6 ± 2.2	3
71	HD200133	6142.0 ± 25	1.498	1.935	3.7	-5.05	4.38 ± 0.04	0.3 ± 0.018	–	3
72	HD202917	5902.0 ± 109	197.725	75.061	19.7	-4.09	5.0 ± 0.11	-0.095 ± 0.076	3.6 ± 1.0	w
73	HD203850	4793.0 ± 52	1.046	1.729	0.5	-4.79	4.43 ± 0.12	-0.68 ± 0.021	–	3

Table C.1: continued.

Index	Star	T_{eff}	RV-RMS	pp Light curves	$v \sin i$	mean($\log(R'_{HK})$)	$\log g$	[Fe/H]	P_{rot}	Sample
74	HD20407	5835.0 ± 16	2.137	0.881	0.5	-4.9	4.46 ± 0.02	-0.44 ± 0.013	–	2,3
75	HD205536	5426.0 ± 20	1.042	0.803	1.4	-5.03	4.31 ± 0.04	-0.05 ± 0.015	3.2 ± 0.9	4
76	HD206683	5945.0 ± 21	1.362	3.065	3.5	-5.05	4.35 ± 0.06	0.24 ± 0.017	–	3
77	HD206998	5775.0 ± 28	2.133	2.099	0.5	-5.01	4.14 ± 0.03	-0.72 ± 0.021	–	1,2,3
78	HD207129	5919.0 ± 13	1.761	6.185	1.9	-4.91	4.43 ± 0.02	-0.02 ± 0.01	–	3
79	HD207869	5480.0 ± 18	1.668	1.511	0.5	-4.96	4.41 ± 0.03	-0.45 ± 0.014	–	24
80	HD20807	5832.0 ± 15	1.896	1.666	1.1	-4.9	4.49 ± 0.03	-0.23 ± 0.012	–	2,3
81	HD209100	4776.0 ± 154	2.287	2.061	1.2	-4.77	4.59 ± 0.39	-0.105 ± 0.057	–	3
82	HD210918	5743.0 ± 10	1.487	0.557	1.2	-5.02	4.3 ± 0.02	-0.1 ± 0.009	–	1,2,3,4
83	HD211415	5839.0 ± 14	2.209	4.479	1.7	-4.97	4.42 ± 0.03	-0.21 ± 0.011	–	3,4
84	HD21161	5916.0 ± 13	1.985	0.886	2.7	-5.06	4.26 ± 0.03	0.09 ± 0.01	–	1
85	HD212036	5683.0 ± 19	6.71	1.003	1.3	-5.05	4.34 ± 0.03	-0.01 ± 0.014	2.5 ± 1.4	2
86	HD21209A	4682.0 ± 46	1.987	5.407	0.5	-4.84	4.5 ± 0.14	-0.41 ± 0.064	38.8 ± 6.9	3
87	HD213042	4709.0 ± 125	2.434	2.428	1.3	-4.88	4.15 ± 0.4	0.165 ± 0.057	–	3
88	HD213628	5553.0 ± 22	0.624	1.66	1.5	-5.0	4.38 ± 0.04	0.01 ± 0.017	–	4
89	HD215456	5797.0 ± 11	3.617	0.789	2.0	-5.09	4.07 ± 0.02	-0.09 ± 0.009	–	2,3
90	HD215906	6219.0 ± 29	0.889	0.666	4.0	-4.91	4.37 ± 0.03	-0.28 ± 0.02	2.3 ± 0.6	3
91	HD216054	5380.0 ± 20	1.081	1.725	0.4	-5.01	4.37 ± 0.04	-0.12 ± 0.015	–	1,2
92	HD218860	5557.0 ± 29	26.463	23.599	6.7	-4.31	4.43 ± 0.05	-0.015 ± 0.022	5.0 ± 2.7	4
93	HD220339	4918.0 ± 40	3.02	4.789	0.6	-4.84	4.31 ± 0.08	-0.31 ± 0.02	–	3
94	HD220507	5672.0 ± 13	1.543	0.735	2.0	-5.07	4.22 ± 0.05	0.01 ± 0.011	–	1,2,3
95	HD221575	5065.0 ± 41	4.806	11.43	3.7	-4.49	4.4 ± 0.09	0.01 ± 0.022	11.0 ± 3.9	w
96	HD221638	6349.0 ± 33	3.124	0.99	4.2	-4.91	4.45 ± 0.04	-0.225 ± 0.023	–	1,2
97	HD222237	4688.0 ± 130	2.985	1.716	0.5	-4.91	4.17 ± 0.27	-0.31 ± 0.188	–	3
98	HD222335	5237.0 ± 32	6.024	0.735	0.5	-4.8	4.4 ± 0.07	-0.16 ± 0.022	–	1,2,3
99	HD222480	5840.0 ± 15	3.932	3.453	2.7	-5.04	4.15 ± 0.04	0.19 ± 0.012	–	1,2,3
100	HD222669	5896.0 ± 15	2.294	2.139	2.5	-4.9	4.45 ± 0.04	0.05 ± 0.012	–	2
101	HD223171	5797.0 ± 14	2.559	0.883	2.5	-5.04	4.09 ± 0.04	0.115 ± 0.011	13.8 ± 5.9	1,2,3
102	HD223681	4995.0 ± 55	62.608	48.955	6.1	-4.05	4.39 ± 0.11	-0.555 ± 0.025	5.6 ± 1.0	2
103	HD224228	4771.0 ± 59	5.262	9.418	2.4	-4.44	4.19 ± 0.15	0.01 ± 0.028	27.2 ± 3.9	w
104	HD224230	4786.0 ± 79	6.436	3.322	1.0	-4.99	4.25 ± 0.19	-0.1 ± 0.037	–	2
105	HD224619	5454.0 ± 19	1.369	2.502	0.9	-4.97	4.4 ± 0.04	-0.2 ± 0.015	15.8 ± 3.9	3
106	HD23249	5120.0 ± 128	2.264	3.408	2.2	-5.21	4.3 ± 0.24	0.09 ± 0.074	–	2,3
107	HD24062	5990.0 ± 19	5.086	4.646	4.6	-5.06	4.22 ± 0.03	0.23 ± 0.015	–	3
108	HD25587	6207.0 ± 29	5.015	2.262	7.2	-5.0	4.26 ± 0.03	-0.12 ± 0.022	23.1 ± 4.1	2
109	HD28471	5730.0 ± 13	1.814	1.775	1.6	-5.0	4.32 ± 0.02	-0.05 ± 0.011	18.7 ± 7.2	2
110	HD30306	5552.0 ± 25	1.427	2.078	2.2	-5.09	4.26 ± 0.05	0.18 ± 0.019	44.8 ± 2.3	2
111	HD3074A	6100.0 ± 17	1.895	0.837	4.0	-5.03	4.39 ± 0.04	-0.01 ± 0.013	12.2 ± 0.7	2,3
112	HD30876	4985.0 ± 47	9.128	10.06	1.7	-4.52	4.36 ± 0.1	-0.085 ± 0.024	9.6 ± 0.8	2
113	HD31822	6016.0 ± 19	5.119	1.059	2.5	-4.86	4.5 ± 0.03	-0.19 ± 0.014	3.6 ± 0.6	3,4
114	HD32564	5518.0 ± 16	3.944	1.884	1.5	-5.02	4.36 ± 0.03	0.08 ± 0.012	–	3
115	HD35854	4788.0 ± 61	1.023	1.238	0.8	-4.82	4.2 ± 0.17	-0.13 ± 0.03	–	3,4
116	HD36003	4558.0 ± 278	3.732	2.226	0.6	-4.89	4.13 ± 0.76	-0.13 ± 0.038	2.4 ± 0.7	3,4
117	HD36379	6026.0 ± 15	1.441	1.726	1.6	-5.0	4.26 ± 0.03	-0.17 ± 0.011	2.8 ± 1.0	2,3
118	HD37990	6201.0 ± 24	4.961	2.348	1.7	-4.75	4.48 ± 0.04	-0.03 ± 0.017	12.3 ± 2.2	3
119	HD3823	6008.0 ± 17	1.807	1.701	1.0	-5.01	4.28 ± 0.04	-0.28 ± 0.013	–	2,3
120	HD38459	5320.0 ± 38	20.766	12.281	0.5	-4.51	4.28 ± 0.1	0.11 ± 0.026	12.0 ± 2.2	2
121	HD38858	5705.0 ± 13	2.098	3.607	0.5	-4.94	4.46 ± 0.03	-0.23 ± 0.01	–	3
122	HD39194	5188.0 ± 17	2.935	1.768	0.5	-4.96	4.47 ± 0.04	-0.61 ± 0.012	20.4 ± 6.5	3
123	HD3964	5723.0 ± 15	3.26	6.874	1.7	-4.9	4.43 ± 0.02	0.05 ± 0.012	–	1,2
124	HD40397	5504.0 ± 18	1.899	3.75	1.1	-5.02	4.35 ± 0.04	-0.13 ± 0.014	2.7 ± 0.5	3,4
125	HD40865	5678.0 ± 18	2.46	1.333	0.5	-4.94	4.39 ± 0.03	-0.38 ± 0.015	–	2,3
126	HD42936	5075.0 ± 60	2.123	2.281	0.5	-5.1	4.18 ± 0.16	0.18 ± 0.039	–	2
127	HD52449	6342.0 ± 23	3.295	1.895	0.5	-4.74	4.49 ± 0.03	0.09 ± 0.017	27.7 ± 5.7	1,2
128	HD53705	5765.0 ± 29	1.26	9.736	1.3	-5.01	4.35 ± 0.05	-0.227 ± 0.023	–	4
129	HD56380	5310.0 ± 25	2.124	3.119	0.5	-5.0	4.3 ± 0.04	-0.42 ± 0.018	–	2,3
130	HD6107	5797.0 ± 13	2.296	0.687	2.3	-5.06	4.04 ± 0.02	-0.055 ± 0.011	13.6 ± 5.8	1,2,3
131	HD65277	4646.0 ± 69	1.132	1.311	0.5	-5.04	4.33 ± 0.17	-0.31 ± 0.03	25.7 ± 4.6	3
132	HD65907A	5911.0 ± 80	1.338	7.067	0.8	-4.94	4.57 ± 0.09	-0.31 ± 0.061	13.8 ± 2.2	3
133	HD67200	6090.0 ± 18	1.843	2.036	3.0	-5.06	4.36 ± 0.04	0.32 ± 0.014	34.1 ± 6.1	2
134	HD69611	5776.0 ± 22	1.69	2.087	0.5	-4.98	4.3 ± 0.03	-0.58 ± 0.017	–	2,3
135	HD71835	5475.0 ± 24	2.957	1.768	1.5	-4.96	4.41 ± 0.04	-0.04 ± 0.017	–	2,3
136	HD72673	5201.0 ± 21	1.319	0.791	0.4	-4.94	4.42 ± 0.04	-0.38 ± 0.015	–	2,3,4
137	HD73524	5979.0 ± 17	1.886	0.981	2.8	-5.03	4.36 ± 0.03	0.15 ± 0.013	–	2,3,4
138	HD74698	5797.0 ± 13	6.49	1.943	2.3	-5.07	4.23 ± 0.03	0.07 ± 0.01	–	1,24
139	HD75881	6094.0 ± 28	8.375	3.554	5.9	-5.15	4.06 ± 0.04	0.07 ± 0.022	–	w
140	HD76849	5285.0 ± 36	1.272	1.75	0.5	-5.04	4.34 ± 0.09	–	–	4
141	HD78429	5738.0 ± 12	3.698	3.201	1.5	-4.93	4.25 ± 0.03	0.089 ± 0.01	34.4 ± 4.2	2,3
142	HD82342	4728.0 ± 607	0.989	1.592	0.5	-5.0	4.23 ± 1.21	-0.54 ± 1.145	30.8 ± 4.9	3
143	HD82516	4998.0 ± 43	1.989	1.536	1.3	-5.01	4.24 ± 0.12	0.01 ± 0.023	10.6 ± 1.9	2,3,4
144	HD85249	6567.0 ± 51	4.04	2.693	12.6	-4.92	4.63 ± 0.07	0.18 ± 0.035	–	3
145	HD85725	6000.0 ± 26	4.187	1.488	6.5	-5.19	4.0 ± 0.05	0.15 ± 0.02	–	w
146	HD87838	5993.0 ± 33	1.888	1.072	0.5	-4.94	4.24 ± 0.03	-0.4 ± 0.023	27.4 ± 4.9	2,3,4
147	HD88218	5845.0 ± 14	4.48	1.785	1.9	-5.05	4.09 ± 0.02	-0.14 ± 0.012	–	3,4
148	HD8828	5386.0 ± 21	1.722	1.072	0.3	-5.01	4.4 ± 0.03	-0.16 ± 0.016	–	2,3

Table C.1: continued.

Index	Star	T_{eff}	RV-RMS	pp Light curves	$v \sin i$	$\text{mean}(\log(R'_{HK}))$	$\log g$	$[Fe/H]$	P_{rot}	Sample
149	HD89839	6245.0 ± 25	1.973	4.409	4.2	-5.01	4.4 ± 0.04	0.04 ± 0.018	–	2
150	HD92719	5794.0 ± 14	4.34	2.368	1.9	-4.85	4.43 ± 0.02	-0.11 ± 0.011	9.5 ± 1.7	4
151	HD93489	5910.0 ± 13	2.21	1.456	2.2	-5.0	4.36 ± 0.02	-0.02 ± 0.011	–	2,3
152	HD94151	5625.0 ± 17	2.131	2.82	1.9	-4.93	4.41 ± 0.03	0.04 ± 0.013	10.6 ± 1.9	3
153	HD94270	5983.0 ± 11	2.443	3.483	1.5	-5.0	4.37 ± 0.02	0.02 ± 0.009	5.9 ± 2.0	3
154	HD94771	5618.0 ± 16	2.93	5.22	3.3	-5.18	3.93 ± 0.04	0.22 ± 0.013	–	2,4
155	HD95456	6292.0 ± 17	2.13	0.927	2.7	-5.02	4.39 ± 0.04	0.16 ± 0.013	–	2,3,4
156	HD96700	5838.0 ± 12	2.847	2.685	0.8	-4.96	4.34 ± 0.02	-0.18 ± 0.01	6.0 ± 1.1	4
157	HD97343	5390.0 ± 26	3.043	1.873	1.4	-5.02	4.32 ± 0.04	-0.055 ± 0.019	–	3,4
158	HIP102152	5706.0 ± 13	2.939	3.455	1.5	-5.02	4.3 ± 0.03	-0.03 ± 0.01	–	2,3
159	HIP105184	5831.0 ± 13	6.028	2.552	2.5	-4.65	4.46 ± 0.02	-0.02 ± 0.011	–	3
160	HIP114328	5778.0 ± 13	2.046	4.235	1.5	-5.03	4.34 ± 0.03	-0.017 ± 0.011	–	4
161	HIP114615	5784.0 ± 16	4.824	3.251	1.6	-4.78	4.4 ± 0.02	-0.057 ± 0.013	24.7 ± 0.4	3,4
162	HIP17157	4534.0 ± 150	13.832	8.864	2.5	-4.64	4.27 ± 0.48	–	15.0 ± 2.7	1,2
163	HIP21934	4507.0 ± 247	17.715	4.513	1.3	-4.93	4.07 ± 0.71	0.03 ± 0.149	30.3 ± 0.9	1,2,3,4
164	HIP22263	5836.0 ± 31	10.863	4.133	3.2	-4.56	4.54 ± 0.06	–	10.6 ± 1.9	2
165	HIP25670	5768.0 ± 12	1.368	1.16	1.8	-4.99	4.39 ± 0.03	0.06 ± 0.009	10.1 ± 1.8	2,3,4
166	HIP28066	5695.0 ± 12	2.0	6.057	1.2	-5.03	4.23 ± 0.02	-0.147 ± 0.01	–	2
167	HIP36515	5801.0 ± 17	13.82	7.731	3.7	-4.42	4.45 ± 0.03	-0.07 ± 0.013	5.3 ± 2.2	2
168	HIP41317	5698.0 ± 11	6.261	1.169	1.4	-5.02	4.37 ± 0.02	-0.081 ± 0.009	–	3
169	HIP54597	4679.0 ± 87	5.441	2.325	0.5	-5.04	4.23 ± 0.23	-0.22 ± 0.04	–	2,3,4
170	HIP68468	5848.0 ± 14	0.341	1.074	2.7	-5.06	4.32 ± 0.03	0.07 ± 0.012	–	3
171	HIP79361	4490.0 ± 226	2.446	7.522	0.6	-4.87	4.11 ± 0.55	0.52 ± 0.467	–	3

¹ using the whole sample² mean $v \sin i$ error: 1.0 [km s⁻¹]³ mean $\log(R'_{HK})$ error: 0.01⁴ subsample classifications, w: only considered in whole sample

Table C.2: List of starts in Fig. 14 with the peak-to-peak of light curve variation < 6.5 ppt and some stellar parameters presents in TIC (Stassun et al. 2018)

TIC ID	Full TOI id	peak-to-peak light curve [ppt]	TESS mag	T_{eff} [K]	R_{star} [R_{Sun}]	$\log g$ [cm s^{-2}]
9033144	367.01	6.02	9.7	5756.9 ± 195.2	1.3 ± 4.0	3.9 ± 0.1
9725627	239.01	5.89	11.0	6362.5 ± 83.0	0.9 ± 1.2	4.6 ± 0.2
9727392	236.01	6.5	11.2	6421.5 ± 83.0	1.5 ± 5.1	4.2 ± 0.2
13021029	439.01	5.4	11.7	6407.0 ± 105.8	1.3 ± 0.5	4.3
14091704	445.01	2.54	9.1	6307.9 ± 124.2	1.6 ± 0.5	4.0 ± 0.1
15445551	747.01	5.89	10.3	6271.0 ± 196.0	1.7 ± 3.0	4.1 ± 0.4
19519368	494.01	4.58	10.0	4985.0 ± 114.0	1.1 ± 3.8	4.7 ± 0.2
22221375	652.01	1.32	7.4	5903.0	1.0 ± 1.4	4.4
22529346	495.01	3.84	10.0	6459.0	1.5 ± 0.1	4.2
23434737	1203.01	1.54	8.0	5742.2 ± 30.4	1.4 ± 0.7	4.3 ± 0.1
25155310	114.01	3.56	10.6	5800.0	1.3 ± 0.1	4.3
29831208	124.01	3.48	11.0	5080.0 ± 181.0	0.9 ± 9.3	4.5 ± 2.0
29960109	393.01	6.14	10.7	3856.0 ± 68.0	0.6 ± 0.3	4.7 ± 0.3
30037565	1209.01	6.01	9.6	5914.0 ± 40.3	1.9 ± 1.9	4.0 ± 0.1
30853470	807.01	4.9	11.2	4662.0 ± 174.0	0.8 ± 2.9	4.6 ± 0.2
31553893	1058.01	4.08	9.3	5785.0 ± 189.0	1.1 ± 3.4	4.3 ± 2.0
33692729	469.01	1.22	8.7	6114.0 ± 194.0	1.0 ± 0.5	4.5 ± 0.3
37575651	568.01	2.2	8.3	5780.0	1.0 ± 1.1	4.4
37749396	260.01	5.68	8.4	4111.0 ± 171.0	0.6 ± 1.5	4.6 ± 0.4
37770169	470.01	2.66	10.6	5418.0 ± 185.0	0.8 ± 1.1	4.6 ± 0.3
38696105	281.01	2.28	10.5	6002.2 ± 42.2	1.5 ± 3.5	4.1 ± 0.1
41227743	804.01	3.52	10.7	5988.0 ± 192.0	1.2 ± 1.6	4.3 ± 2.0
42054565	280.01	3.54	10.0	5454.0 ± 185.0	0.8 ± 4.8	4.6 ± 0.3
43647325	423.01	3.63	10.4	5904.0 ± 156.8	1.1 ± 0.8	4.4
47384844	1022.01	4.87	8.7	6084.0 ± 111.0	1.4 ± 0.8	4.1 ± 0.3
47911178	471.01	2.73	9.8	6400.0	1.3 ± 0.1	4.3
48476907	658.01	2.53	9.4	6521.0 ± 199.0	1.5 ± 19.9	4.2 ± 2.0
48476908	659.01	2.49	9.5	5990.0 ± 192.0	1.7 ± 17.9	4.0 ± 0.7
49687222	254.01	5.37	9.8	6101.0 ± 193.0	1.0 ± 4.5	4.5 ± 0.4
49899799	416.01	3.41	8.3	6084.8 ± 35.2	1.9 ± 0.2	4.0 ± 0.3
50309953	1109.01	2.14	9.8	5317.0 ± 65.7	0.9 ± 2.7	4.5 ± 0.1
50312495	1211.01	2.62	9.8	5572.9 ± 104.0	1.2 ± 2.2	3.8 ± 0.2
50618703	544.01	3.84	9.6	4665.0 ± 177.0	0.7 ± 0.4	4.7 ± 0.3
52204645	209.01	6.34	10.8	4892.0 ± 179.0	0.8 ± 4.1	4.5 ± 2.0
53189332	660.01	3.75	11.0	6055.0	1.4 ± 0.3	4.2
53735810	661.01	4.3	11.2	6580.0	1.8 ± 0.3	4.1
54085154	662.01	2.56	8.2	6380.0 ± 80.0	1.3 ± 0.5	4.4
55559618	695.01	5.45	10.7	5591.0 ± 187.0	1.1 ± 3.4	4.4 ± 2.0
61538902	752.01	6.32	11.3	5900.0	0.9 ± 0.2	4.5
70513361	262.01	0.76	8.1	5302.6 ± 21.0	0.8 ± 0.7	4.5
70914192	427.01	3.34	10.3	5271.7 ± 43.7	1.1 ± 4.3	4.3 ± 0.4
73228647	755.01	2.82	9.5	6003.0 ± 192.0	1.0 ± 0.8	4.5 ± 0.3
76989773	182.01	2.62	9.6	5569.0 ± 187.0	1.1 ± 5.7	4.3 ± 0.3
89020549	132.01	4.81	10.8	5673.0 ± 188.0	0.9 ± 1.6	4.6 ± 0.4
94986319	421.01	4.01	9.2	5718.0 ± 189.0	1.1 ± 6.4	4.4 ± 2.0
96097215	728.01	4.47	10.3	5272.0 ± 183.0	0.9 ± 4.7	4.4 ± 2.0
100100827	185.01	2.44	8.8	6400.0	1.2	4.4
101230735	1060.01	3.83	9.6	5687.9 ± 76.0	1.3 ± 6.0	4.6 ± 0.1
101955023	667.01	4.14	10.9	3202.0	0.3 ± 0.8	4.9
103633434	1235.01	2.69	9.9	3912.0 ± 157.0	0.6 ± 0.2	4.6
106402532	733.01	4.2	8.8	5969.0 ± 192.0	1.0 ± 1.1	4.5 ± 0.3
111991770	820.01	4.8	10.4	6300.0	1.5 ± 0.1	4.2
116483734	1412.01	6.46	11.1	4223.4 ± 133.4	0.7 ± 11.3	4.6 ± 0.1
117979897	443.01	6.05	12.0	5928.0 ± 114.4	1.4 ± 0.5	4.3
119700084	1413.01	4.77	10.1	5427.0 ± 141.3	0.9 ± 8.7	4.5 ± 0.1
120602501	1366.01	3.07	8.5	5705.0 ± 185.1	1.7 ± 5.4	4.0 ± 0.1
120610833	229.01	6.0	11.4	5100.0	0.9 ± 0.2	4.5
120960812	1237.01	3.49	10.3	6212.0 ± 132.8	1.5 ± 4.1	4.2 ± 0.1
122612091	264.01	1.9	10.5	6250.0	2.0 ± 0.1	4.0
123702439	499.01	1.9	10.1	5997.0 ± 192.0	1.0 ± 1.6	4.5 ± 0.3
124573851	669.01	2.81	10.1	5581.9 ± 76.0	1.2 ± 0.6	4.1 ± 0.1
126733133	570.01	5.39	10.0	5973.0 ± 192.0	1.3 ± 4.4	4.3 ± 0.3
127530399	822.01	6.41	11.1	4775.0	0.7 ± 0.2	4.6
128790976	1124.01	1.86	7.2	6541.0 ± 94.0	1.6 ± 4.7	4.2 ± 0.1
131081852	758.01	4.91	9.9	6072.0 ± 193.0	1.3 ± 19.4	4.3 ± 2.0
131419878	720.01	1.15	8.8	6482.3 ± 205.2	1.5 ± 0.3	4.2 ± 0.4
134537478	501.01	4.55	10.4	5720.0	1.5 ± 0.1	4.2
138588540	1434.01	5.57	8.1	5393.9 ± 139.7	0.7 ± 0.9	4.7 ± 0.1
140068425	140.01	6.47	9.8	6174.0 ± 194.0	1.3 ± 5.1	4.3 ± 2.0
140760434	1229.01	5.38	10.7	6028.8 ± 44.1	2.0 ± 3.8	4.0 ± 0.1
141527965	1216.01	5.87	11.4	4280.0 ± 171.0	0.7 ± 0.4	4.6 ± 0.2
143350972	440.01	1.27	7.7	5759.2 ± 38.2	1.0 ± 0.1	4.4

Table C.2: continued.

TIC ID	Full TOI id	peak-to-peak light curve	TESS mag	T_{eff}	R_{star}	$\log g$
144065872	105.01	4.56	9.5	5630.0	1.1 ± 0.1	4.4
147950620	1194.01	3.25	10.5	5339.9 ± 155.2	1.0 ± 0.5	4.4 ± 0.1
148782377	1415.01	2.84	8.4	6383.0 ± 130.4	1.4 ± 0.6	4.2 ± 0.1
149301575	809.01	4.56	10.3	5804.3 ± 76.0	1.3 ± 1.0	3.9 ± 0.1
149603524	102.01	2.37	9.7	6280.0	1.3	4.3
150030205	286.01	1.72	9.1	5245.0 ± 183.0	0.8 ± 1.7	4.6 ± 0.3
150098860	220.01	5.38	9.7	5272.7 ± 45.6	0.9 ± 1.9	4.0 ± 0.1
153065527	406.01	4.14	11.2	3349.0 ± 63.0	0.3 ± 0.7	4.9 ± 0.4
153976959	1435.01	4.15	10.0	5142.0 ± 122.7	0.8 ± 2.4	4.5 ± 0.1
154089169	1174.01	5.29	10.3	5029.5 ± 59.9	0.8 ± 0.2	4.6 ± 0.1
154383539	1436.01	3.86	11.1	5011.2 ± 102.7	0.7 ± 1.9	4.6 ± 0.1
154840461	1153.01	2.35	8.4	6528.3 ± 179.4	1.7 ± 0.5	4.2 ± 0.1
158002130	1180.01	2.55	10.1	4738.1 ± 139.3	0.7 ± 0.2	4.6 ± 0.1
158025009	1416.01	2.17	9.1	4946.0 ± 128.6	0.8 ± 1.8	4.5 ± 0.1
158623531	246.01	3.55	11.2	5070.0	0.9 ± 0.1	4.5
158978373	823.01	2.91	10.0	6309.0 ± 196.0	1.4 ± 1.1	4.2 ± 0.3
159510109	1141.01	6.31	8.9	5894.7 ± 90.3	1.1 ± 0.3	4.4 ± 0.1
159951311	265.01	4.21	11.7	5310.0	0.8 ± 0.2	4.6
160074939	230.01	1.79	8.7	6467.0 ± 198.0	1.6 ± 1.6	4.2 ± 0.3
160148385	247.01	4.87	11.9	5540.0	1.0 ± 0.2	4.4
166739520	190.01	1.56	9.6	6038.0	1.2 ± 0.1	4.4
166836920	267.01	1.27	8.9	6180.0	1.8 ± 0.1	4.1
167303382	802.01	1.56	7.5	5235.8 ± 28.6	0.8 ± 0.4	4.4
167342439	707.01	5.55	10.1	5409.2 ± 41.8	1.0 ± 1.7	4.5 ± 0.1
167415965	214.01	1.73	8.0	5346.2 ± 12.9	0.9 ± 0.4	4.5
167754523	409.01	4.84	9.1	4913.8 ± 71.5	0.8 ± 0.1	4.5 ± 0.2
170102285	477.01	5.05	11.7	5150.0	0.8 ± 0.1	4.6
172193428	502.01	3.76	10.3	5642.0 ± 188.0	1.4 ± 1.5	4.2 ± 0.3
175180796	816.01	4.7	11.1	4146.6 ± 148.6	0.6 ± 1.1	4.6 ± 0.1
176778112	408.01	5.84	9.6	5600.0 ± 187.0	1.0 ± 5.9	4.4 ± 0.3
177258735	801.01	1.34	7.5	6283.4 ± 44.4	1.6 ± 0.4	4.4
179317684	163.01	3.55	10.8	6387.9 ± 196.4	1.7 ± 1.0	4.2 ± 2.0
183120439	169.01	6.23	11.7	5780.6 ± 401.1	1.3 ± 1.5	4.3 ± 2.0
183537452	192.01	2.65	10.2	4800.0	0.8 ± 0.1	4.5
183985250	193.01	4.66	9.1	5422.0 ± 185.0	1.0 ± 1.4	4.4 ± 0.3
184952758	719.01	2.59	9.0	5761.2 ± 89.8	0.9 ± 0.1	4.5 ± 0.3
188768068	1462.01	0.72	5.9	5801.9 ± 124.6	1.3 ± 1.3	4.3 ± 0.1
190990336	585.01	3.74	8.9	6118.1 ± 137.4	1.7 ± 0.9	4.3 ± 0.3
198212955	1242.01	4.35	11.6	4255.0 ± 128.2	0.7 ± 2.8	4.6 ± 0.1
198241702	1269.01	3.21	10.9	5591.0 ± 185.0	0.8 ± 0.4	4.4
198356533	1437.01	2.39	8.7	6093.0 ± 124.7	1.2 ± 0.7	4.3 ± 0.1
198390247	1453.01	2.31	10.1	4920.0 ± 127.0	0.7 ± 1.6	4.6 ± 0.1
199688472	1292.01	3.65	9.8	5672.9 ± 168.9	1.5 ± 6.6	4.1 ± 0.1
200807066	869.01	2.93	8.9	5908.0 ± 191.0	1.2 ± 2.6	4.3 ± 0.3
201793781	248.01	2.8	8.4	5711.7 ± 57.0	1.2 ± 0.7	3.8 ± 0.1
206466531	410.01	2.47	10.0	6000.2 ± 130.8	1.5 ± 0.2	4.4 ± 0.1
207081058	121.01	4.51	9.9	6053.0 ± 193.0	1.2 ± 2.2	4.3 ± 0.3
207084429	381.01	0.78	7.2	5883.0 ± 52.4	1.9 ± 0.2	–
211438925	194.01	3.69	10.2	5940.0	1.4 ± 0.1	4.2
219239945	701.01	2.74	10.9	5837.0 ± 190.0	1.1 ± 0.7	4.4 ± 0.3
219338557	133.01	4.54	9.9	4028.0 ± 170.0	0.7 ± 1.9	4.6 ± 0.2
219379012	397.01	4.52	10.2	5973.5 ± 185.9	1.0 ± 2.5	3.9 ± 0.1
219388773	399.01	5.22	10.6	4752.8 ± 64.0	1.0 ± 0.5	4.4 ± 0.1
219698950	766.01	5.49	11.5	5870.0	1.0 ± 0.1	4.4
219850915	1244.01	5.37	11.0	4599.0 ± 123.0	0.7 ± 2.1	4.6 ± 0.1
220396259	379.01	2.29	9.9	5825.0 ± 97.8	1.7 ± 0.2	4.0 ± 0.1
224297258	1279.01	2.68	10.0	5477.0 ± 120.1	0.8 ± 2.0	4.6 ± 0.1
229650439	1438.01	4.09	10.3	5374.0 ± 183.0	0.8 ± 0.3	6.0 ± 0.3
229770036	1348.01	5.24	10.7	4567.0 ± 143.3	0.8 ± 0.2	4.4 ± 0.1
230017324	1280.01	4.07	10.6	4665.0 ± 128.1	0.7 ± 2.5	4.6 ± 0.1
230088370	1176.01	2.2	10.2	6557.7 ± 83.3	1.6 ± 0.4	4.2 ± 0.1
230982885	195.01	1.58	10.0	5640.0	1.1 ± 0.1	4.4
231912935	215.01	4.17	10.5	5821.0 ± 190.0	1.0 ± 1.7	4.4 ± 0.3
232025086	874.01	2.15	8.8	6437.0 ± 198.0	1.4 ± 1.3	4.2 ± 0.3
232540264	1247.01	1.49	8.5	5711.8 ± 106.3	1.1 ± 0.6	4.4 ± 0.1
232612416	1248.01	3.79	11.1	5227.0 ± 119.5	0.9 ± 0.6	4.5 ± 0.1
232967440	1173.01	2.39	10.3	5429.6 ± 292.5	1.0 ± 0.5	4.4 ± 0.1
232971294	1281.01	2.46	9.7	6191.0 ± 127.5	1.3 ± 1.4	4.3 ± 0.1
232976128	1249.01	2.67	10.2	5453.0 ± 117.9	1.0 ± 2.3	4.4 ± 0.1
232982558	1439.01	1.94	10.0	5873.0 ± 123.8	1.6 ± 0.9	4.0 ± 0.1
233087860	1184.01	5.62	9.9	4681.4 ± 80.5	0.7 ± 1.1	4.6 ± 0.1
233390838	1341.01	2.25	9.5	6477.6 ± 101.6	1.7 ± 5.4	4.1 ± 0.1
233541860	1486.01	2.44	10.0	4154.0 ± 173.4	0.6 ± 0.1	4.5 ± 0.1
233617847	1440.01	4.07	9.6	5780.0	1.0 ± 0.9	4.4
233681149	1340.01	2.96	10.8	5929.0 ± 124.8	1.0 ± 0.4	4.5 ± 0.1

Table C.2: continued.

TIC ID	Full TOI id	peak-to-peak light curve	TESS mag	T_{eff}	R_{star}	log g
233684822	1253.01	2.08	9.9	5779.0 ± 188.0	1.5 ± 3.2	4.9 ± 0.4
233951353	1441.01	2.02	9.5	5885.0 ± 201.6	1.2 ± 1.4	4.3 ± 0.1
234345288	213.01	3.34	9.7	4566.4 ± 64.0	0.7 ± 1.1	4.9 ± 0.1
236714379	1254.01	3.13	10.8	5451.0 ± 125.9	1.1 ± 0.9	4.3 ± 0.1
237222864	1255.01	3.04	9.1	5126.0 ± 124.4	0.9 ± 0.5	4.5 ± 0.1
237232044	1443.01	2.52	9.9	5236.0 ± 125.3	0.7 ± 0.5	4.6 ± 0.1
238176110	116.01	3.61	11.0	4920.0	0.9 ± 0.1	4.5
238197638	903.01	5.37	11.7	6266.0 ± 41.0	1.4 ± 2.0	4.3 ± 0.2
240968774	1467.01	6.01	10.6	3834.0 ± 157.0	0.5 ± 2.4	4.7
243200602	826.01	4.95	10.5	5625.0	1.0 ± 0.1	4.5
248075138	769.01	5.9	11.3	5315.0	0.9 ± 0.2	4.5
250386181	390.01	4.45	9.9	6321.5 ± 53.5	1.1 ± 6.5	4.2 ± 0.1
253990973	1061.01	4.12	9.7	5525.0 ± 186.0	1.2 ± 0.6	4.3 ± 0.3
255685030	799.01	4.42	10.5	5643.0 ± 188.0	1.0 ± 3.5	4.5 ± 0.3
257567854	403.01	6.04	11.2	6153.0	1.2 ± 0.2	4.3
258514800	1444.01	4.17	10.2	5466.0 ± 121.5	0.9 ± 3.4	4.5 ± 0.1
258777137	1183.01	4.93	9.9	5095.6 ± 1241.5	1.1 ± 0.2	–
259511357	271.01	2.53	8.4	6025.0 ± 192.0	1.2 ± 1.5	4.3 ± 0.4
259592689	429.01	2.74	10.2	5160.7 ± 90.5	1.0 ± 0.4	4.4 ± 0.2
259701242	401.01	3.79	8.2	5928.0 ± 85.6	1.0 ± 0.1	4.5 ± 0.2
260043723	217.01	4.65	8.7	6278.0 ± 196.0	1.7 ± 1.3	4.1 ± 0.3
260708537	486.01	3.47	9.3	3445.0 ± 87.0	0.4 ± 1.0	4.9 ± 0.1
261257684	904.01	5.75	10.8	3992.0 ± 170.0	0.6 ± 1.0	4.6 ± 0.2
261867566	905.01	5.65	10.5	5565.0 ± 187.0	1.0 ± 1.8	4.5 ± 0.3
263003176	130.01	1.79	7.4	6295.7 ± 56.5	1.1 ± 1.1	4.4
264979636	518.01	5.27	10.1	5596.0 ± 187.0	1.1 ± 4.2	4.3 ± 0.3
266980320	118.01	1.68	9.2	5586.0 ± 187.0	1.1 ± 0.6	4.4 ± 0.3
268644785	505.01	2.85	10.7	6003.0	1.5 ± 0.1	4.2
270341214	173.01	1.52	8.9	6409.0 ± 197.0	1.5 ± 1.3	4.2 ± 0.3
271168962	828.01	6.22	9.4	6030.0	1.5 ± 0.1	4.1
271893367	150.01	3.26	10.9	5766.0 ± 37.3	1.6 ± 0.3	4.1 ± 0.1
271900960	389.01	2.91	8.3	6457.7 ± 115.5	1.4 ± 2.6	4.4 ± 0.3
272635712	1349.01	2.25	9.3	5711.1 ± 365.0	1.3 ± 0.4	4.2 ± 0.1
273985865	1208.01	3.83	10.5	5626.0 ± 188.0	0.9 ± 2.3	4.6 ± 0.3
274138511	506.01	3.15	10.4	5280.0 ± 183.0	0.9 ± 3.1	4.4 ± 2.0
277103955	284.01	3.21	9.2	4779.8 ± 128.6	0.7 ± 0.1	4.6 ± 0.3
277507814	1286.01	4.42	10.2	6588.0 ± 247.6	1.6 ± 3.1	4.2 ± 0.1
277683130	138.01	5.77	9.5	5722.0 ± 189.0	1.1 ± 8.3	4.4 ± 2.0
279425357	739.01	6.5	11.5	6083.6 ± 125.0	1.2 ± 2.6	4.3 ± 0.2
280095254	235.01	2.79	9.3	5454.4 ± 77.3	1.0 ± 5.8	3.4 ± 0.1
280206394	677.01	4.18	9.2	6446.0 ± 198.0	1.2 ± 1.5	4.4 ± 0.3
280830734	188.01	2.48	9.4	6340.3 ± 204.0	1.6 ± 7.5	4.2 ± 0.3
281575427	205.01	2.2	9.4	6222.5 ± 83.0	1.5 ± 2.7	4.1 ± 0.2
286132427	635.01	4.94	8.1	5914.0 ± 191.0	1.0 ± 0.9	4.5 ± 0.3
287156968	1230.01	1.69	9.6	5696.0 ± 188.0	1.2 ± 1.1	4.3 ± 0.3
288132261	1258.01	5.71	9.1	6124.0 ± 126.6	1.5 ± 0.4	4.2 ± 0.1
290131778	123.01	1.22	8.8	6188.0 ± 194.0	1.3 ± 7.7	4.3 ± 2.0
290348383	1099.01	4.49	7.4	4867.0 ± 179.0	1.0 ± 0.6	4.4
294301883	774.01	6.17	11.3	6070.0	1.1 ± 0.1	4.4
294471966	1446.01	5.04	10.8	5180.0 ± 101.3	0.8 ± 2.1	4.5 ± 0.1
294781547	1218.01	3.68	10.3	5456.0 ± 48.9	1.0 ± 2.9	4.5 ± 0.1
294981566	1219.01	6.24	10.1	6734.0 ± 202.0	1.6 ± 2.1	4.2 ± 0.4
299799658	1062.01	4.04	9.4	5394.0 ± 185.0	0.9 ± 0.5	4.5 ± 0.3
300293197	211.01	5.7	9.4	5874.0 ± 102.6	1.1 ± 6.4	4.4 ± 0.1
304042899	775.01	2.71	9.5	6746.0 ± 202.0	1.2 ± 8.5	4.4 ± 0.4
306362738	479.01	2.9	10.8	5600.0	1.0 ± 0.1	4.4
309791156	533.01	5.76	10.9	4666.1 ± 64.0	1.1 ± 1.7	4.2 ± 0.1
314865962	208.01	3.96	10.3	5493.0 ± 186.0	1.0 ± 1.3	4.4 ± 0.3
317060587	1052.01	2.74	9.0	5958.2 ± 76.0	1.6 ± 4.5	4.3 ± 0.1
317548889	480.01	1.05	6.8	6212.6 ± 49.0	1.6 ± 1.8	4.4
320004517	1055.01	2.73	8.1	5783.5 ± 7.8	1.1 ± 0.6	4.5
321857016	1420.01	4.48	11.2	5387.0 ± 136.6	0.9 ± 0.7	4.5 ± 0.1
322063810	253.01	1.78	9.3	4020.0 ± 170.0	0.6 ± 1.6	4.4
325680697	414.01	3.1	9.1	5773.7 ± 76.0	1.3 ± 5.3	3.5 ± 0.1
327301957	1074.01	2.9	10.6	5206.0 ± 183.0	0.8 ± 0.5	4.6 ± 0.3
335499997	680.01	5.44	9.0	5967.0 ± 192.0	1.8 ± 1.4	3.9 ± 0.4
339672028	481.01	4.4	9.4	5760.0 ± 189.0	1.7 ± 1.6	4.0 ± 0.3
339733013	417.01	4.24	10.0	5834.2 ± 179.5	1.3 ± 0.3	4.2 ± 0.1
339857675	686.01	2.26	9.9	6279.8 ± 127.2	1.6 ± 0.3	4.3 ± 0.4
346418409	1423.01	5.63	10.9	4993.0 ± 127.1	0.7 ± 7.7	4.7 ± 0.1
348844154	916.01	5.23	11.2	5493.2 ± 126.6	1.9 ± 1.2	3.9 ± 0.5
349827430	1148.01	1.51	7.9	6403.9 ± 184.1	1.5 ± 0.9	4.2 ± 0.1
350153977	908.01	3.68	10.6	5500.0 ± 76.0	1.1 ± 3.9	5.0 ± 0.1
350584963	787.01	3.81	9.5	6623.0 ± 200.0	1.3 ± 2.3	4.4 ± 0.3
350743714	165.01	2.67	9.8	6038.0 ± 54.0	1.9 ± 2.1	4.0 ± 0.1

Table C.2: continued.

TIC ID	Full TOI id	peak-to-peak light curve	TESS mag	T_{eff}	R_{star}	$\log g$
352413427	1473.01	2.73	8.3	5958.0 ± 121.3	1.0 ± 0.5	4.5 ± 0.1
352764091	1287.01	1.81	8.6	5891.0 ± 124.6	1.2 ± 1.7	4.3 ± 0.1
354594208	1492.01	3.45	9.8	5904.0 ± 249.1	1.2 ± 0.4	4.3 ± 0.1
358460246	867.01	4.07	10.4	5777.4 ± 113.6	1.2 ± 1.0	4.3 ± 0.2
359271092	741.01	5.51	7.7	3766.0 ± 95.0	0.5 ± 0.7	4.8 ± 0.1
364107753	909.01	1.0	7.0	6059.1 ± 50.4	1.6 ± 0.8	4.3 ± 0.1
364186197	1408.01	2.4	8.8	6594.0 ± 90.9	1.6 ± 0.6	4.2 ± 0.2
364393429	1207.01	2.92	9.2	6282.0 ± 196.0	1.2 ± 1.0	4.4 ± 0.3
365733349	1288.01	3.15	9.9	6180.0 ± 362.0	0.9 ± 0.4	4.6 ± 0.1
366989877	1054.01	1.64	8.4	6122.0 ± 194.0	1.2 ± 0.9	4.3 ± 0.3
369327947	910.01	4.38	10.3	3194.0 ± 101.0	0.3 ± 1.3	5.0 ± 0.1
373844472	275.01	4.27	11.0	5616.0 ± 187.0	1.1 ± 18.7	4.4 ± 2.0
374829238	785.01	6.3	11.5	3783.0	1.0 ± 0.2	4.4
374997123	1222.01	3.37	10.3	6082.0 ± 193.0	1.2 ± 2.4	4.3 ± 0.3
375059587	786.01	2.54	9.8	5853.8 ± 45.2	1.4 ± 1.2	4.2 ± 0.1
377293776	1450.01	3.14	10.0	3407.0 ± 157.0	0.5 ± 2.6	4.8
382188882	276.01	3.75	10.6	6366.0 ± 197.0	1.5 ± 5.3	4.2 ± 0.5
382437043	1223.01	4.81	9.3	6516.0 ± 199.0	1.9 ± 3.0	4.0 ± 0.4
382474101	349.01	4.08	10.2	6054.0 ± 193.0	1.2 ± 14.0	4.3 ± 2.0
382626661	283.01	5.09	9.6	5250.0 ± 183.0	0.7 ± 0.9	4.6 ± 0.3
386435344	575.01	2.4	8.7	6529.0 ± 199.0	1.9 ± 13.5	4.0 ± 0.3
387259626	1455.01	3.87	10.2	6458.8 ± 157.5	1.4 ± 0.9	4.3 ± 0.1
391949880	128.01	1.79	7.9	6086.0 ± 193.0	1.3 ± 0.9	4.3 ± 0.3
393414358	483.01	2.35	10.4	5570.0	1.9 ± 0.2	4.0
394657039	159.01	3.44	10.5	6404.0 ± 463.3	1.6 ± 3.1	4.4 ± 0.2
394698182	170.01	6.4	11.9	5768.2 ± 56.4	1.2 ± 0.4	4.3 ± 2.0
399144800	1213.01	3.59	10.6	6270.0 ± 196.0	1.0 ± 1.9	4.5 ± 0.4
402026209	232.01	5.69	11.8	5436.0	0.9 ± 0.1	4.5
403224672	141.01	1.19	7.4	5795.3 ± 44.6	1.2 ± 0.4	4.4
406941612	912.01	3.81	10.4	3566.0 ± 66.0	0.4 ± 0.4	4.8 ± 0.4
407126408	913.01	5.4	9.6	4948.0 ± 180.0	0.7 ± 1.0	4.6 ± 0.3
407966340	554.01	1.7	6.4	6337.9 ± 44.7	1.8 ± 0.9	4.4
408159788	420.01	3.67	10.6	5747.3 ± 518.8	0.8 ± 0.4	4.6 ± 0.3
408310006	576.01	5.23	8.8	6313.0 ± 196.0	1.3 ± 0.8	4.3 ± 0.3
410245915	725.01	5.31	10.2	6173.3 ± 152.9	0.8 ± 0.2	4.2 ± 2.0
415969908	233.01	5.1	11.3	3644.0 ± 64.0	0.5 ± 0.6	4.8 ± 0.4
417676622	1290.01	2.17	9.5	5875.2 ± 137.9	1.3 ± 3.0	4.3 ± 0.1
417931607	1451.01	3.53	9.0	5781.0 ± 130.5	1.0 ± 2.1	4.4 ± 0.1
418959198	1424.01	5.14	10.5	4529.0 ± 104.6	0.8 ± 3.3	4.5 ± 0.1
421894914	1056.01	4.96	9.7	6124.3 ± 83.0	1.4 ± 1.0	4.4 ± 0.2
424865156	1265.01	2.82	10.0	6532.2 ± 109.2	2.0 ± 0.7	4.0 ± 0.1
427348923	484.01	5.54	11.6	4425.0 ± 90.0	0.7 ± 1.2	4.6 ± 0.1
432549364	1476.01	3.99	10.2	6596.0 ± 156.6	1.5 ± 0.6	4.2 ± 0.1
437242640	744.01	2.7	9.7	5700.0	0.9 ± 0.3	4.5
437248515	683.01	4.82	11.4	6302.0	1.2 ± 0.1	4.3
440100539	1548.01	2.9	8.7	5891.9 ± 92.3	1.2 ± 0.2	4.3 ± 0.1
445859771	1273.01	5.9	10.4	5736.0 ± 164.8	1.1 ± 4.6	4.4 ± 0.1
451606970	1214.01	2.03	10.0	5262.4 ± 76.0	1.1 ± 2.0	4.0 ± 0.1
453211454	509.01	1.69	7.9	5560.3 ± 43.4	1.0 ± 0.5	4.4
453260209	1215.01	6.03	9.6	3751.0 ± 68.0	0.5 ± 1.0	4.8 ± 0.3
455135327	490.01	4.15	9.9	6304.0	1.2 ± 0.1	4.4
458478250	1165.01	2.79	9.8	5787.0 ± 109.9	1.0 ± 0.6	4.5 ± 0.1
459942762	430.01	1.86	8.2	5997.7 ± 78.3	1.0 ± 0.1	–
459969957	1274.01	6.28	11.9	4968.1 ± 172.4	0.8 ± 0.5	4.5 ± 0.1
467666275	1204.01	5.16	8.0	6711.0 ± 201.0	1.8 ± 2.6	4.1 ± 0.3
468148930	1086.01	5.26	12.2	5818.0 ± 190.0	1.1 ± 8.3	4.3 ± 2.0
1400770435	1344.01	1.64	8.9	5941.5 ± 161.9	1.4 ± 1.3	4.2 ± 0.1